VII. PLASMA ELECTRONICS*

Prof. L. D. Smullin
Prof. H. A. Haus
Prof. A. Bers
Prof. W. D. Getty
Prof. D. J. Rose
Prof. T. H. Dupree
Prof. L. M. Lidsky
Prof. E. P. Gyftopoulos
Dr. G. Fiocco
F. Alvarez de Toledo
W. L. Brassert
R. J. Briggs
J. R. Cogdell
L. J. Donadieu
S. A. Evans
E. T. Gerry
B. A. Hartenbaum
H. Y. Hsieh
G. I. Kachen
P. K. Karvellas
J. D. Levine
L. N. Lontai
D. L. Morse
R. T. Nowak
L. M. Petrie, Jr.
W. D. Rummler
A. J. Schneider
P. E. Serafim
P. S. Spangler
G. Theodoridis
E. Thompson
C. E. Wagner
S. Wilensky
H. L. Witting
J. C. Woo

A. BEAM-PLASMA DISCHARGE

When a strong electron beam is sent through a partially evacuated region, a series of events occurs that have led us to coin the name "beam-plasma discharge." By this we mean a dynamic process in which plasma is produced by electrons that have been accelerated in microwave fields, and the microwaves in turn have been generated by the strong interaction between the beam and the plasma.[1] The interaction between the beam and plasma is such that intense microwave oscillations are produced either in the neighborhood of the electron cyclotron frequency or of the electron plasma frequency, ω_p. The oscillations are accompanied by large oscillatory velocities of the plasma electrons. When these velocities become large enough, the plasma electrons will further ionize the ambient gas, thus shifting ω_p and the oscillation frequency.

Simultaneous with the ionization process, considerable rf emission and light emission occur and large ion currents appear at the walls of the cylindrical waveguide. Some of the plasma electrons are accelerated to very high energies by the fields in the discharge. This is inferred from the x-rays emitted by the walls and by a molybdenum target, as well as from the large negative floating potential of a probe placed near the beam.

1. Plasma Electron Energy

Four different types of measurements have been used to determine the electron energy in the plasma.

(a) An average electron temperature has been calculated from measurements of ion currents leaving the plasma volume, and of the loss of power by the electron beam. In the steady state, the equation of continuity is

---

*This work was supported in part by the National Science Foundation (Grant G-24073); in part by the U.S. Navy (Office of Naval Research) under Contract Nonr-1841(78); and in part by Purchase Order DDL B-00368 with Lincoln Laboratory, a center for research operated by Massachusetts Institute of Technology with the joint support of the U. S. Army, Navy, and Air Force under Air Force Contract AF 19(604)-7400.

$$I_+ = I_- = n_- e \nu_i v_p, \tag{1}$$

where I_+ is the total ion current, I_- is the total electron current leaving the plasma volume v_p, n_- is the plasma density, and ν_i is the ionization frequency.

The power balance equation is approximately

$$f I_o V_o = P_i + I_- T_-, \tag{2}$$

where fI_oV_o is the fraction of the beam power (I_oV_o) given to the plasma, P_i is the power lost in ionization and excitation processes, and I_-T_- is the power lost because of electrons leaving the plasma volume, and T_- is the mean energy of the electrons in volts.

If we neglect excitation losses

$$P_i = \nu_i n_- e V_i v_p, \tag{3}$$

where V_i is the ionization potential. With the use of Eqs. 1 and 3, Eq. 2 becomes

$$I_+(T_- + V_i) = f I_o V_o. \tag{4}$$

In a typical experiment on system B with helium gas[2] used:

$f = 0.3$

$V_i = 24.6$ volts

$I_+ = 6.6$ amps

$I_o = 1$ amp

$V_o = 10,000$ volts.

Then

$T_- \approx 430$ volts.

(b) The presence of high-energy plasma electrons has also been inferred from measurements of x-rays emitted by a molybdenum target. The target (1 in. × 1.5 in. × 0.01 in.) is movable, and experiments were performed with the target far from the beam (Fig. VII-1). At low pressures when a beam-plasma discharge cannot be sustained, no x-rays are observed. In the presence of the discharge x-rays are observed with the target parallel to the beam axis but the intensity is weak. With the target at 45° with respect to the beam axis, in either direction, the x-rays observed are considerably

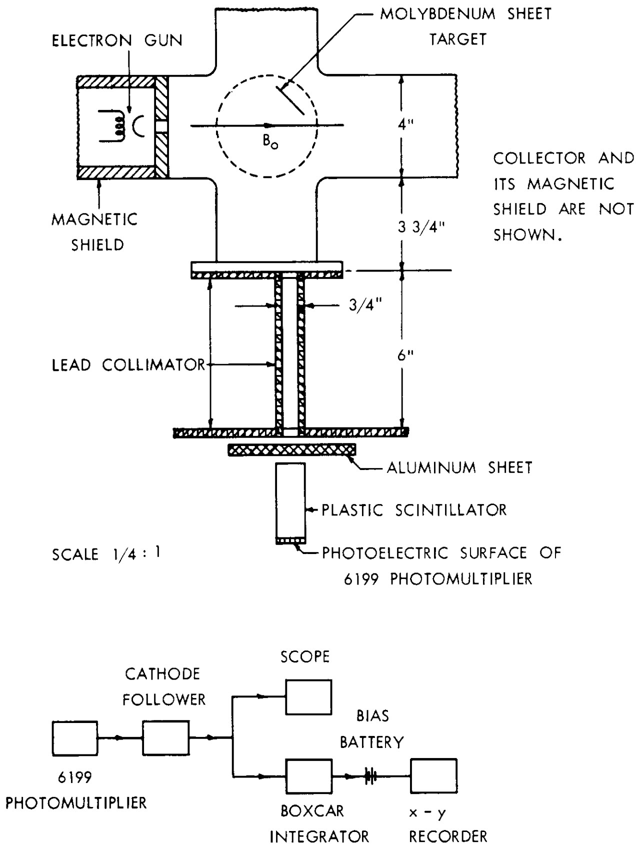

Fig. VII-1. Experimental geometry and schematic of x-ray absorption measurements in system A.

more intense. The results of a specific set of measurements are given in Fig. VII-2. These are for a beam voltage of 10 kv, with the target oriented 45° to the beam axis. By adjusting pressure and magnetic field for maximum x-ray intensity, we have been able to make absorption experiments with varying thicknesses of aluminum sheet up to 0.180 inch thick. The log of the observed intensities when plotted against the thickness of the absorber gave an average slope that falls between the K_β line of molybdenum (19.5 kv) and K_α line of tin (25.1 kv) as shown in Fig. VII-2. (The collimator resolution was such that both the target and the tin-coated wall were visible to the scintillator detector.) The measurement indicates the presence of electrons of approximately 20-kv energy or twice the beam voltage.

(c) The presence of high-energy electrons is also inferred from measurements of probe floating potential. The instantaneous voltage between a Langmuir probe and ground was measured at various positions in the discharge. The probe was grounded through a 1-megohm voltage divider. The time constant was approximately 1 μsec. A typical variation of floating potential with position at a given axial position is shown in

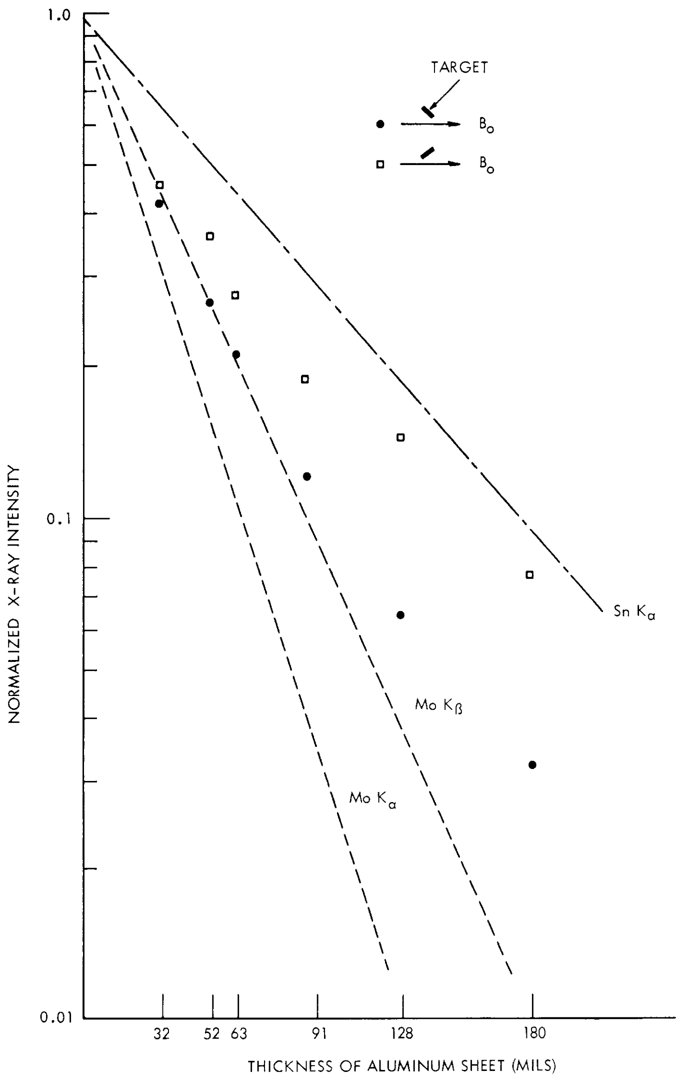

Fig. VII-2. Plot of normalized x-ray intensity vs thickness of aluminum sheet. Helium gas pressure, 0.2 μ Hg; magnetic mirror, 2:1; central field, 600 gauss; beam voltage, 10 kv.

Fig. VII-3. Negative floating potentials in excess of 1000 volts were observed when the beam voltage was 5.6 kv; this observation indicates the presence of high-energy electrons.

(d) Another estimate of the average electron energy was made by comparing the intensities of two He I lines. The light was observed just after the beam was turned off. Preliminary measurements indicate an electron temperature of 30-100 ev, but there are several conditions in the experiment which may not satisfy the assumed theoretical conditions.[3] Work will continue on this method to determine the validity of these preliminary results.

2. Electron Density

The plasma density ranges from 10^{11}/cc to 10^{13}/cc. This was estimated in two ways. First, the highest, strongest emitted frequency (that is not a harmonic of some lower emitted frequency) was assumed to equal ω_p, which is proportional to $n_-^{1/2}$. Second, the density was estimated from the average total charge flowing to the walls after the beam pulse had ended and from an estimate of the plasma volume.[2]

3. Plasma Ion Energy

In a typical helium beam-plasma discharge, the width of the 4686 Å line was found to be 0.4 Å. If this observed broadening were caused entirely by thermal motion of the ions, the ion temperature would be 5 ev. The plasma ion can acquire energy from the microwave fields, from the dc fields, or through collisional heating. The microwave and dc fields still have to be measured, but the fact that a positive floating potential is

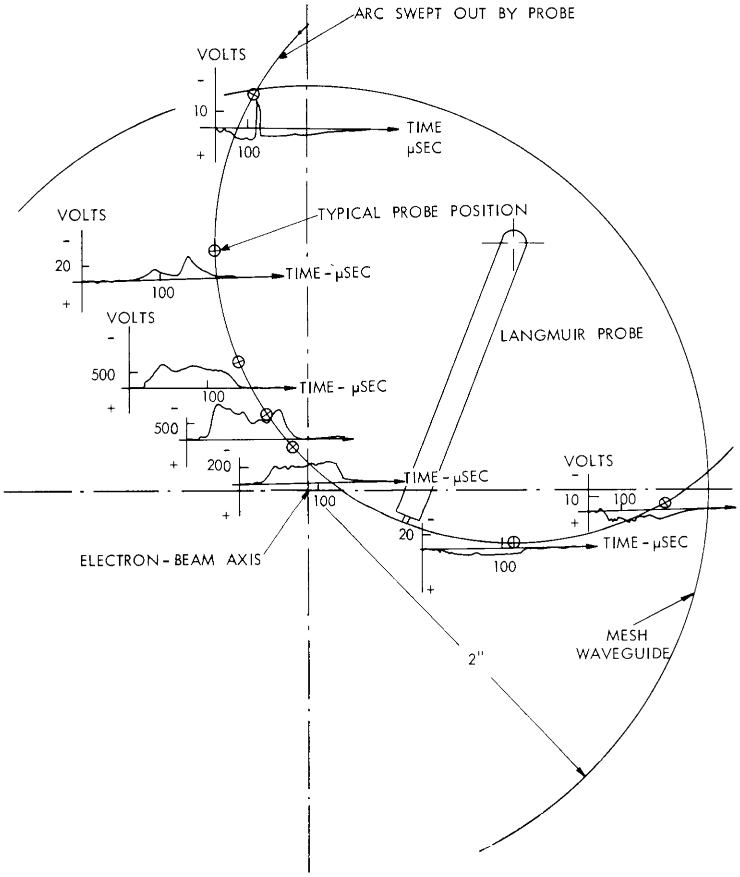

Fig. VII-3. Floating potential vs times at various positions in system A. Hydrogen gas pressure, 0.2 μ Hg; magnetic mirror, 2:1; central field, 600 gauss; beam voltage, 5.6 kv.

frequently observed near the walls (see Fig. VII-3) suggests that ions are expelled from the plasma by a large space potential between the discharge and the walls. This space-charge electric field may have been responsible for the spread of ion velocities inferred from the spectral broadening.

It can be shown that collisional heating of the ions by the electrons, competing with losses that are due to charge exchange and to loss of ions from the mirror, cannot produce an ion temperature of this magnitude, given our neutral particle density of 7×10^{12}/cc.

L. D. Smullin, W. D. Getty, B. A. Hartenbaum, H. Y. Hsieh

References

1. L. D. Smullin and W. D. Getty, Generation of a hot, dense plasma by a collective beam-plasma interaction, Phys. Rev. Letters 9, 3-6 (July 1, 1962).

2. L. D. Smullin, B. A. Hartenbaum, and H. Y. Hsieh, Electron beam plasma interaction experiments, Quarterly Progress Report No. 67, Research Laboratory of Electronics, M.I.T., October 15, 1962, pp. 71-76.

3. S. P. Cunningham, Spectroscopic Observations, U.S. AEC Technical Report WASH-289, University of California Radiation Laboratory, Livermore, California, June 1955, p. 279.

B. INSTABILITY IN THE HOLLOW-CATHODE DISCHARGE

An instability in the hollow-cathode discharge[1] has been observed which may be associated with the diffusion of plasma across the magnetic field away from the arc. We observe a single broad "spoke" of plasma rotating about the axis of the discharge. The density and shape of this cloud has been studied, and its behavior with various arc parameters is being observed. A theoretical study of the problem is being made.

1. Behavior of the Plasma Cloud

Our experimental arrangement is shown in Fig. VII-4. The arc is run on the magnetic axis of the system in argon at a pressure of several times 10^{-4} mm Hg. The magnetic field may be varied continuously up to approximately 600 gauss, and arc currents in the range 5-20 amps are used.

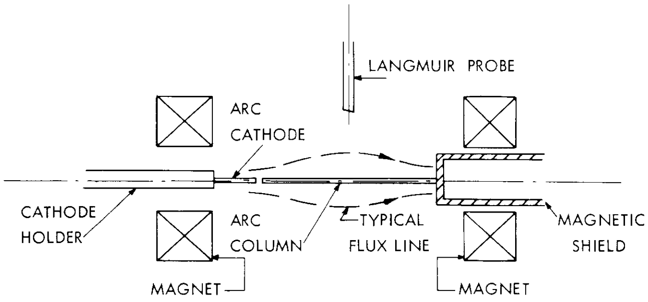

Fig. VII-4. Experimental arrangement.

The plasma cloud has been studied with a pair of movable Langmuir probes. The density and shape of the cloud has been approximately determined from ion saturation current and temperature, and the frequency of rotation of the cloud has been plotted against various parameters. We observe that the instability only appears for magnetic

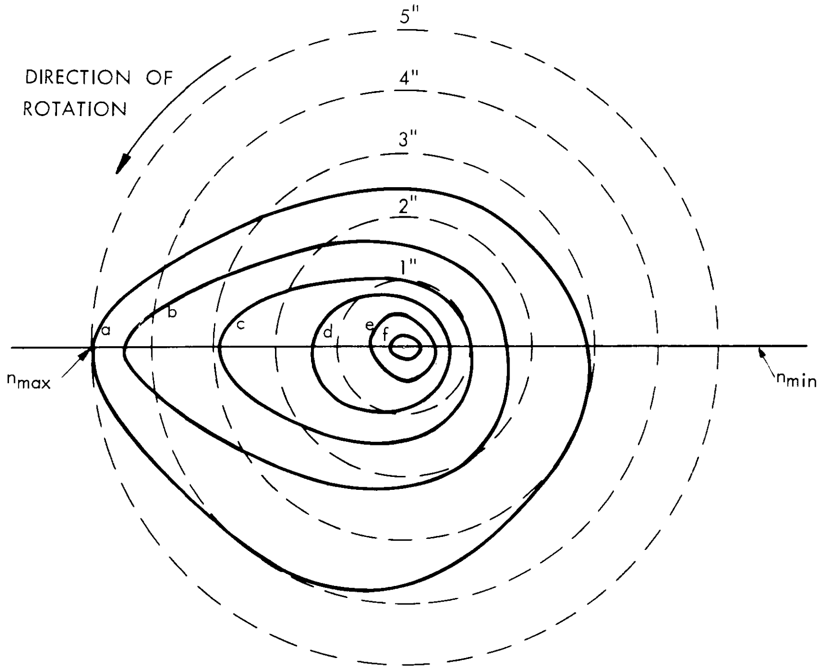

Fig. VII-5. Density Contour Map. Density in particles per cm^3: a, 10^{10}; b, 2×10^{10}; c, 4×10^{10}; d, 8×10^{10}; e, 1.8×10^{11}; f, 2.5×10^{11}. Magnetic field into the page.

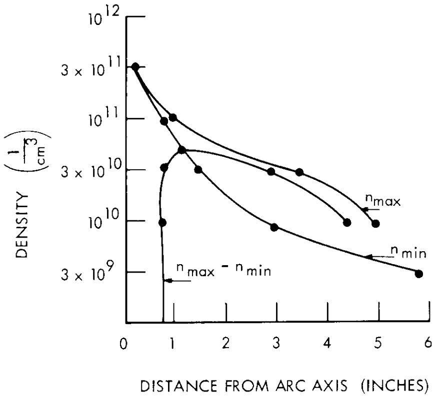

Fig. VII-6. Density profiles of disturbance.

fields above a certain value, which is not a strong function of pressure or arc current.

Figure VII-5 is a density contour map, each contour corresponding to a constant density at an instant of time. The whole map rotates counterclockwise at a few kilocycles. It is observed that the cloud does not exhibit any helical pattern, that is, there is no measurable phase shift of the density maximum with distance along the axis.

Figure VII-6 shows density profiles taken along the lines marked n_{max} and n_{min} on the contour map. Also, $n_{max}-n_{min}$ is plotted on the same axis.

Figure VII-7 illustrates the variations in rotational frequency with magnetic field and with arc current. The frequency is approximately proportional to the square root of magnetic field, and increases with increasing arc current. Figure VII-8 shows that the relation between the period of rotation and the background pressure is nearly linear.

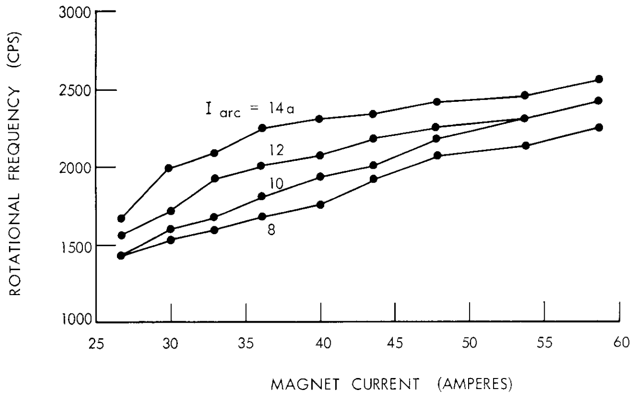

Fig. VII-7. Rotational frequency of disturbances vs magnet current, with arc current a parameter. Magnetic field on axis, approximately 10 gauss per ampere magnet current.

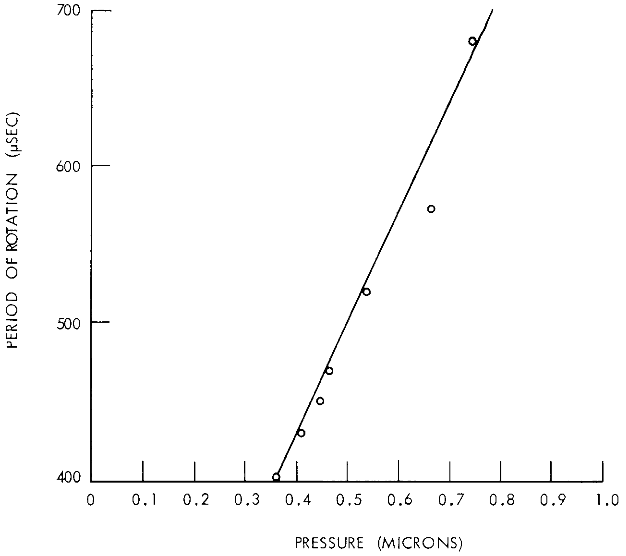

Fig. VII-8. Effect of background pressure on rotational period. Magnet current, 40 amps; arc current, 10 amps.

2. Theoretical Considerations

We postulate that the frequency of rotation of the cloud is such that the azimuthal velocity of the particles is equal to the (E_r/B_z) drift velocity. The direction of rotation agrees with this hyphothesis, since the plasma potential is positive with respect to the vacuum-chamber walls, thereby indicating an outward radial electric field. In a reflex discharge the plasma is contained between the cathode and a reflector, both between 50 and 80 volts negative with respect to the vacuum-chamber walls. In this case the sense of rotation of the cloud is observed to be opposite to that in the straight (nonreflex) arc. The frequency of rotation is almost right for the values of E_r and B_z in the system, and has no relation to a cyclotron frequency of any type of particle present.

Although we have not yet established the mechanisms for this instability, we are trying to compare our observations with those predicted for the "flute" instability and for the helical instability of Kadomtsev and Nedospasov.[2]

D. L. Morse

References

1. D. L. Morse, Electron beam-plasma interaction experiments, Quarterly Progress Report No. 64, Research Laboratory of Electronics, M.I.T., January 15, 1962, pp. 93-94.

2. B. B. Kadomtsev and A. V. Nedospasov, Instability of the positive column in a magnetic field and the 'anomalous' diffusion effect, J. Nuclear Energy, Part C, Vol. 1, pp. 230-235, 1960.

C. COUPLING OF EMPTY-WAVEGUIDE MODES, ELECTROSTATIC AND MAGNETOSTATIC MODES IN WAVEGUIDES LOADED WITH GYROTROPIC MEDIA

In this report we present a new approach to the solution of wave propagation in gyrotropic waveguides. Chorney used an argument based on coupling between an empty-waveguide mode and a quasi-static mode for the interpretation of a particular dispersion curve obtained by computations based on the exact determinantal equation.[1] Bers suggested the examination of the coupling of empty-waveguide and electrostatic modes for plasma-loaded waveguides. We now present the details of this approach and illustrate its use. Recently a similar coupling-of-modes approach was used in the solution of ferrite and plasma waveguides, as suggested by Auld.[2,3] However, the details of that approach are quite different from ours, as will be pointed out here.

1. Uncoupled Modes

Consider a gyrotropic medium characterized by dielectric and magnetic permittivity tensors

$$\overline{\overline{K}} = \begin{pmatrix} K_\perp & jK_x & 0 \\ -jK_x & K_\perp & 0 \\ 0 & 0 & K_{||} \end{pmatrix} \tag{1}$$

$$\overline{\overline{L}} = \begin{pmatrix} L_\perp & jL_x & 0 \\ -jL_x & L_\perp & 0 \\ 0 & 0 & L_{||} \end{pmatrix}. \tag{2}$$

We analyse $\overline{E}$ and $\overline{H}$ in a rotational and an irrotational part:

$$\overline{E} = \overline{E}^r - \nabla\Phi \tag{3a}$$

$$\overline{H} = \overline{H}^r - \nabla\Psi \tag{3b}$$

We expand $\overline{E}^r$ and $\overline{H}^r$ into series of empty-waveguide modes, and Φ and Ψ into series of electrostatic and magnetostatic modes. We then substitute these expansions in Maxwell's equations for the gyrotropic medium. The coupling of these modes because of the gyrotropic nature of the medium will then be established with the aid of the orthogonality relation for the individual modes. The orthogonality relations for electrostatic modes are

$$\gamma_\ell^2 \int K_{||}\Phi_\ell\Phi_m^* \, da = \delta_{\ell m} \tag{4a}$$

$$\int \nabla_T\Phi_m^* \cdot \overline{\overline{K}}_T \cdot \nabla_T\Phi_\ell \, da = \delta_{\ell m}, \tag{4b}$$

and for the magnetostatic modes are

$$\gamma_m^2 \int L_{||}\Psi_m\Psi_\ell^* \, da = \delta_{m\ell} \tag{5a}$$

$$\int \nabla_T\Psi_\ell^* \cdot \overline{\overline{L}}_T \cdot \nabla_T\Psi_m \, da = \delta_{m\ell}. \tag{5b}$$

The main difference with Auld and Eidson's treatment lies in the characterization of each quasi-static mode, not by its propagation constant (γ_m) but by other variables (plasma frequency in the case of plasma, radian frequency in the case of ferrite).

2. Coupled-Mode Theory

We define

$$\hat{E}_T^r = \sum_i V_i\hat{e}_{Ti} \tag{6a}$$

$$\hat{H}^r_T = \sum_i I_i \hat{h}_{Ti} \tag{6b}$$

$$\Phi = \sum_i F_i \Phi_i \tag{7}$$

$$\Psi = \sum_i M_i \Psi_i. \tag{8}$$

Substituting Eqs. 6-8 in Maxwell's equations and applying the orthogonality relations, we obtain

$$\gamma(\bar{V}+\bar{\bar{a}}\,\bar{F}) = \bar{\bar{b}}\,\bar{I} + \bar{\bar{c}}\,\bar{M} \tag{9a}$$

$$\gamma(\bar{I}+\bar{\bar{d}}\,\bar{M}) = \bar{\bar{e}}\,\bar{V} + \bar{\bar{f}}\,\bar{F} \tag{9b}$$

$$\bar{F} = \frac{\bar{\bar{f}}^\dagger}{j\omega\epsilon_o}\,\bar{V} + \frac{\gamma\bar{\bar{a}}^\dagger}{j\omega\epsilon_o}\,\bar{I} \tag{10}$$

$$\bar{M} = \frac{\bar{\bar{c}}^\dagger}{j\omega\mu_o}\,\bar{I} + \frac{\gamma\bar{\bar{d}}^\dagger}{j\omega\mu_o}\,\bar{V}. \tag{11}$$

Here, the dagger means complex conjugate of the transpose of a matrix, and

$$a_{i\ell} = p_{ei}^2 \int \phi_i^* \Phi_\ell \, da \tag{12a}$$

$$b_{in} = \frac{1}{j\omega\epsilon_o} p_{en}^2 p_{ei}^2 \int \frac{\phi_i^* \phi_n}{K_\parallel}\, da + j\omega\mu_o \int \hat{h}^*_{Ti} \cdot \bar{\bar{L}}_T \cdot \hat{h}_{Tn}\, da \tag{12b}$$

$$c_{im} = j\omega\mu_o \int \hat{h}^*_{Ti} \cdot \bar{\bar{L}}_T \cdot (-\nabla_T \Psi_m)\, da \tag{12c}$$

$$d_{im} = p_{hi}^2 \int \psi_i^* \cdot \Psi_m \, da \tag{12d}$$

$$e_{in} = \frac{1}{j\omega\mu_o} p_{hi}^2 p_{hn}^2 \int \frac{\psi_i^* \psi_n}{L_\parallel}\, da + j\omega\epsilon_o \int \hat{e}^*_{Ti} \cdot \bar{\bar{K}}_T \cdot \hat{e}_{Tn}\, da \tag{12e}$$

$$f_{i\ell} = j\omega\epsilon_o \int \hat{e}^*_{Ti} \cdot \bar{\bar{K}}_T \cdot (-\nabla_T \Phi_\ell)\, da. \tag{12f}$$

Lower-case letters for potentials denote the empty-waveguide modes; and upper-case letters, the quasi-static modes. The symbol p denotes transverse wave numbers.

3. Discussion

If we consider all of the empty-waveguide modes, the quasi-static modes (Eqs. 10 and 11) are eliminated, and we get the equations of Chorney.[1] This is to be expected, since the empty-waveguide modes form a complete set. When we do not consider the complete set of empty-waveguide modes, the first two of Maxwell's equations are satisfied only approximately, and the divergence equations must be satisfied independently; hence Eqs. 10 and 11 are then independent of Eqs. 9a and 9b.

In the case of a waveguide completely filled by a dielectric medium each electrostatic potential is related to only one transverse electromagnetic potential $\left(\Phi_\ell = \frac{1}{\sqrt{K_\perp}}\phi_\ell\right)$. Therefore the quasi-static modes are eliminated in our treatment. This does not happen for ferrite-loaded waveguides. There is coupling of each magnetostatic potential to more than one transverse electromagnetic potential, which is due to the boundary conditions.

Our treatment is, however, most useful for partially filled waveguides. We assume that the characteristic tensors are different from 1 in the space occupied by the gyrotropic medium, and equal to 1 in the free space outside the medium. The formulation given here allows for the tensors to be functions of the transverse coordinates, and hence the results also apply directly to the partially filled waveguide.

4. Example

For a completely filled circular cylindrical plasma waveguide of radius a we examine the coupling among the TE_{10} mode, TM_{10} mode, and the $Q.S._1$ mode. There exists a magnetostatic field along the axis of the waveguide. The propagation constant is determined by the determinant of Eqs. 9 and 10. The dominant term in the expansion of this determinant contains the three assumed modes and leads to the following approximate expression for the propagation constant:

$$\gamma^2 = -u^2K_\perp + \frac{1}{2}\left(p_{h1}^2 + \frac{K_\perp}{K_\parallel}p_{e1}^2\right)$$
$$\pm\frac{1}{2}\left[\left(\frac{K_\perp}{K_\parallel}p_{e1}^2 - p_{h1}^2\right)^2 + 3.2\,\frac{K_x^2}{K_\parallel}u^2\left(K_\parallel u^2 - p_{e1}^2\right)\right]^{1/2} \tag{13}$$

The frequencies are normalized over $\omega_N = c/a \cdot (u = \omega/\omega_N)$, and the propagation constants over $k_N = 1/a$.

Equation 11 gives the following expressions for cutoffs $(u_{ec};u_{hc})$:

$$u_{ec}^2 - u_p^2 = p_{e1}^2 \qquad \text{(E-cutoffs)} \tag{14a}$$

$$u_{hc}^2\,\frac{K_\perp^2 - 0.8K_x^2}{K_\perp} = p_{h1}^2 \qquad \text{(H-cutoffs).} \tag{14b}$$

The only difference from the exact expressions is the numerical coefficient 0.8 that appears in Eq. 14b.

For the resonances we find

Cyclotron resonances ($u = u_{ci}$ or u_{ce})

$$\frac{\gamma^2}{K_\perp} \longrightarrow -1.9u^2 + \frac{p_{el}^2}{K_\parallel}. \tag{15}$$

In the exact solution[4] we have 2.0 instead of 1.9.

Plasma resonance ($u = u_{p0}$)

$$\gamma^2 K_\parallel \longrightarrow p_{el}^2 K_\perp \tag{16}$$

which is identical with the exact solution.[4]

These expressions include the change from forward waves to backward waves at cyclotron resonance.

P. E. Serafim, A. Bers

References

1. P. Chorney, Sc.D. Thesis, Department of Electrical Engineering, M.I.T., September 1961.
2. B. A. Auld, Internal Memorandum M. L. No. 931, Microwave Laboratory, Stanford University, June 1962.
3. B. A. Auld and J. C. Eidson, Internal Memorandum M. L. No. 964, Microwave Laboratory, Stanford University, October 1962.
4. W. P. Allis, S. J. Buchsbaum, and A. Bers, Waves in Anisotropic Plasmas (The M.I.T. Press, Cambridge, Mass., 1963).

D. ION OSCILLATIONS IN NEUTRALIZED, THIN ELECTRON BEAMS

In this report we present a possible theoretical explanation of the mechanism for inducing ion oscillations in thin electron beams. The instability is of a "hose" type ($n = \pm 1$) in which the ac velocity of the beam is largely in the transverse direction.

Consider a thin cylindrical electron beam of radius b partially or fully neutralized by an ion background of the same radius. It is assumed that there are no stationary electrons. The beam moves with dc velocity v_o parallel to a magnetic field B_o, both in the z direction. We assume that the metal drift-tube radius is much larger than b.

For such a thin beam, a quasi-static treatment is justified when the beam is nonrelativistic. We consider the angular dependences $e^{jn\phi}$ with $n = \pm 1$, and look for wave solutions of the form $e^{j(\omega t - \beta z)}$. If we take the small-argument limit of the appropriate

Bessel functions, the potentials in the vicinity of the beam are

$$\begin{aligned} \phi_i &= K\frac{r}{b}\,e^{\pm j\phi} && \text{inside} \\ \phi_o &= K\frac{b}{r}\,e^{\pm j\phi} && \text{outside.} \end{aligned} \tag{1}$$

If we equate the discontinuity in the normal electric field to the surface charge, we obtain the following dispersion equation

$$\frac{\omega_{pb}^2}{\omega_r(\omega_r \pm \omega_{ce})} + \frac{\omega_{pi}^2}{\omega(\omega \mp \omega_{ci})} = 2, \tag{2}$$

where $\omega_r = \omega - \beta v_o$, ω_{pb} is the beam-plasma frequency, ω_{pi} is the ion-plasma frequency, ω_{ce} is the electron-cyclotron frequency, and ω_{ci} is the ion-cyclotron frequency. The beam waves in the absence of the ions are shown in Fig. VII-9. We see that for $\omega_{pb} \ll \omega_{ce}$, we have the usual cyclotron and synchronous waves of a filamentary beam. The dispersion in the presence of the ions is sketched in Fig. VII-10 for $\omega_{pi} \gg \omega_{ci}$. We see that there are convective instabilities for both $n = \pm 1$ which have an infinite rate of growth in space for $\omega = \omega_{pi}/\sqrt{2}$. This instability can be interpreted as a coupling of the "generalized" cyclotron and synchronous waves because of the ions. It is a type of reactive-medium amplification in the sense that the ion "oscillators" appear inductive just below the resonant frequency $\omega_{pi}/\sqrt{2}$.

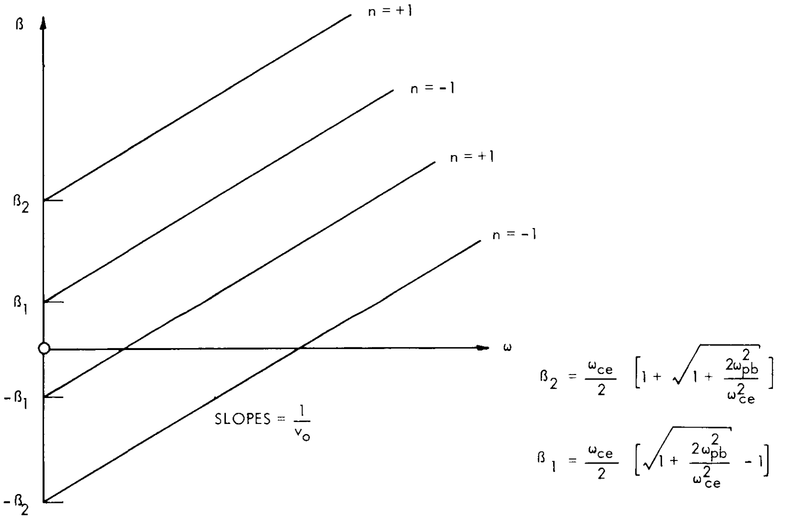

Fig. VII-9. Electron-beam waves in the absence of ions.

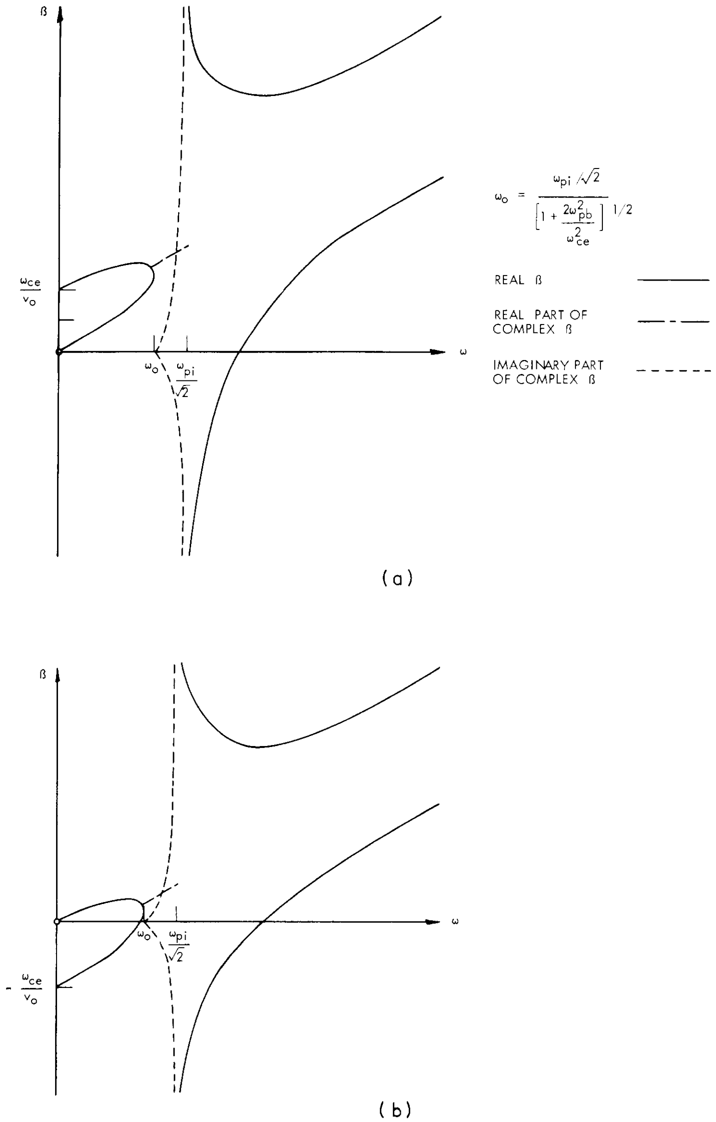

Fig. VII-10. Electron beam-ion interaction.
(a) n = +1; (b) n = −1.

We should note that the infinite gain violates the assumption of $\beta b \ll 1$; however, a gain that is comparable to 1/b is extremely large.

R. J. Briggs

E. ELECTRON-CYCLOTRON PLASMA HEATING

Investigations on the production of hot dense plasmas by microwaves at the electron-cyclotron frequency (Quarterly Progress Report No. 64, pages 103-104, and No. 65, pages 95-97) have been resumed. An experiment at medium power is being carried out (Fig. VII-11); it utilizes an RK 62 pulsed magnetron at λ = 10 cm, and a cylindrical cavity with concave end plates. This cavity is made of copper-plated stainless steel and has a volume of approximately 25 liters, so that it has a high mode density in the neighborhood of 3000 mc. Preliminary experiments were made with 1-μsec pulses at

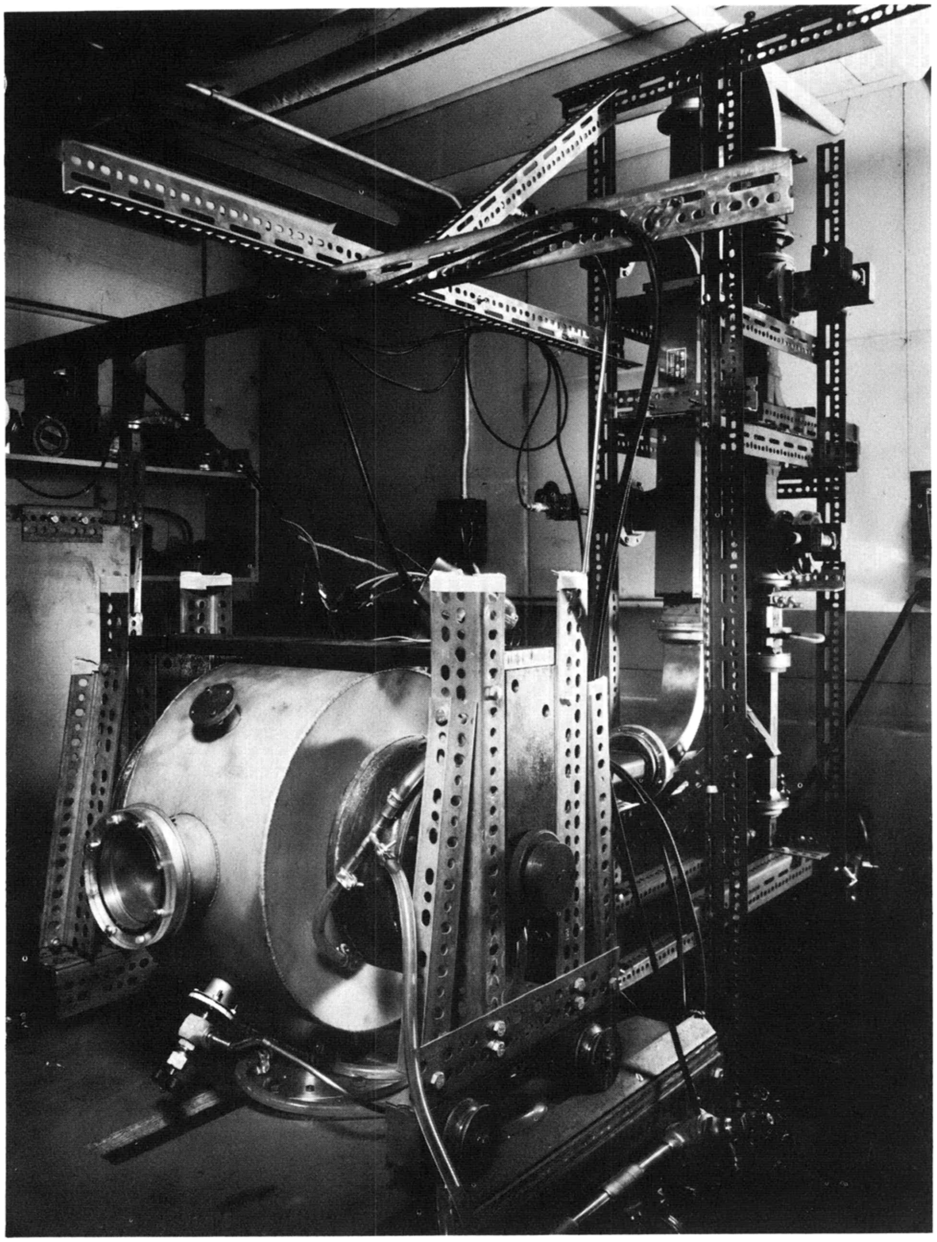

Fig. VII-11. Cavity and waveguide assembly.

a 500/sec repetition rate, and available peak power of 50-60 kw produced visible discharges at air pressures of approximately 10^{-4} mm Hg, with x-ray intensity of tens of kilovolts.

G. Fiocco, L. D. Smullin

F. ELECTRON-BEAM INTERACTIONS WITH IONS IN A WARM PLASMA

A theoretical study is being made of the various beam-plasma instabilities in a warm plasma in order to determine the feasibility of heating ions directly from a collective type of interaction. In this report we summarize some results of a one-dimensional analysis of the problem.

We consider the one-dimensional system of an unbounded electron beam moving with velocity v_o through an unbounded plasma parallel to an applied steady magnetic field, B_o (both taken to be in the z direction). The waves along the magnetic field have the dependence $\exp[j(\omega t-kz)]$; these waves split into the longitudinal and transverse waves, which are uncoupled and therefore can be considered separately.

1. Longitudinal Interaction

The longitudinal waves have only a longitudinal component of the electric field and zero magnetic field. The dispersion equation can be written

$$\frac{\omega_{pb}^2}{(\omega-kv_o)^2} = K_{\parallel}(\omega, k), \tag{1}$$

where ω_{pb} is the beam-plasma frequency and $K_{\parallel}$ is the longitudinal dielectric constant of the plasma. From a collisionless kinetic treatment, assuming cold ions, one obtains[1]

$$K_{\parallel} = 1 - \frac{\omega_{pi}^2}{\omega^2} - \omega_{pe}^2 \int_{-\infty}^{\infty} \frac{f_o(v_z)\, dv_z}{(\omega-kv_z)^2}, \tag{2}$$

where f_o is the unperturbed velocity distribution and ω_{pi} and ω_{pe} are the ion- and electron-plasma frequencies, respectively. From a transport equation model, assuming an isotropic pressure, one has[1]

$$K_{\parallel} = 1 - \frac{\omega_{pi}^2}{\omega^2} - \frac{\omega_{pe}^2}{\omega^2 - k^2V_{Te}^2}, \tag{3}$$

where V_{Te} is the average thermal velocity of the plasma electrons. It can be shown that the two formulations give identical results when (ω/k) is either much larger or much smaller than V_{Te}, even though they are derived from quite different physical assumptions.

a. Weak Beam

For a beam density that is much less than the plasma density, to solve for the beam waves we can set $k = (\omega/v_o) + \delta$ and assume that $\delta \ll \omega/v_o$. Therefore,

$$K_{\|}(\omega, k) \approx [K_{\|}]_{\omega=kv_o} + \left[\frac{\partial K_{\|}}{\partial k}\right]_{\omega=kv_o} \delta. \tag{4}$$

A necessary, but not sufficient, condition for the validity of this approximation is that $(n_b/n_p)(T_e/2V_o) \ll 1$, where n_b and n_p are the beam and plasma densities, T_e is the electron temperature, and V_o is the voltage corresponding to the beam velocity v_o. For $T_e/V_o \ll 1$, much stronger conditions on n_b/n_p are required.

For the transport equation model, Eq. 3, we see that a convective instability is obtained in the regions in which $[K_{\|}]_{\omega=kv_o}$ is negative, and that the maximum spacial growth rate occurs near the synchronism of the plasma wave with the beam ($[K_{\|}]_{\omega=kv_o} = 0$). The mechanism here is the well-known reactive-medium amplification: when a bunched electron beam passes through a medium with a negative dielectric constant (an "inductive medium"), the electrons in a bunch attract rather than repel and hence the bunching is further enhanced. In Fig. VII-12 the regions in which $K_{\|} < 0$ are plotted in the ω-k plane. We see that for $2V_o > T_e$ the maximum amplification occurs above ω_{pe}. This amplification has been considered by a number of authors.[2] For $(m/M)T_e < 2V_o < T_e$, there is no instability. For $2V_o < (m/M)T_e$, there is again amplification, which now is a maximum at a frequency less than ω_{pi}; the growth rate in space is

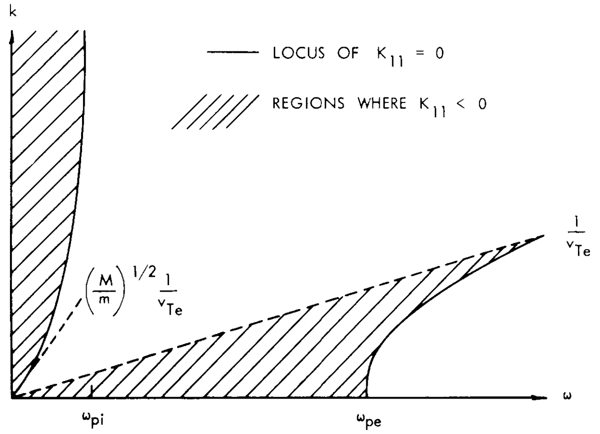

Fig. VII-12. Regions in which $K_{\|} < 0$.

$$\mathrm{Im}\,k = \frac{3^{1/2}}{2^{4/3}} \frac{\omega_{pi}}{v_o} \left(\frac{n_b}{n_p} \frac{T_e}{2V_o}\right)^{1/3} \left(1 - \frac{M}{m} \frac{2V_o}{T_e}\right)^{1/2}, \tag{5}$$

which is less than ω_{pi}/v_o for the conditions assumed here.

The collisionless kinetic treatment, Eq. 2, gives similar results except in the region in which $2V_o$ is comparable to T_e. The dielectric constant $[K_{||}]_{\omega=kv_o}$ is now complex; it can be shown that this fact leads to a convective instability even in the region in which $2V_o < T_e$. The mechanism for the instability is now of a "resistive-medium" type[3]; the novel feature in the present analysis is that the loss in the medium comes about because of the Landau damping. This amplification is plotted in Fig. VII-13 for a Maxwellian distribution of velocities. The frequency of maximum gain is of the order of $(2V_o/T_e)^{1/2}$ ω_{pe} for $2V_o < T_e$; however, the peak of the gain decreases rapidly if $2V_o/T_e$ is decreased, since the Landau damping is then much less.

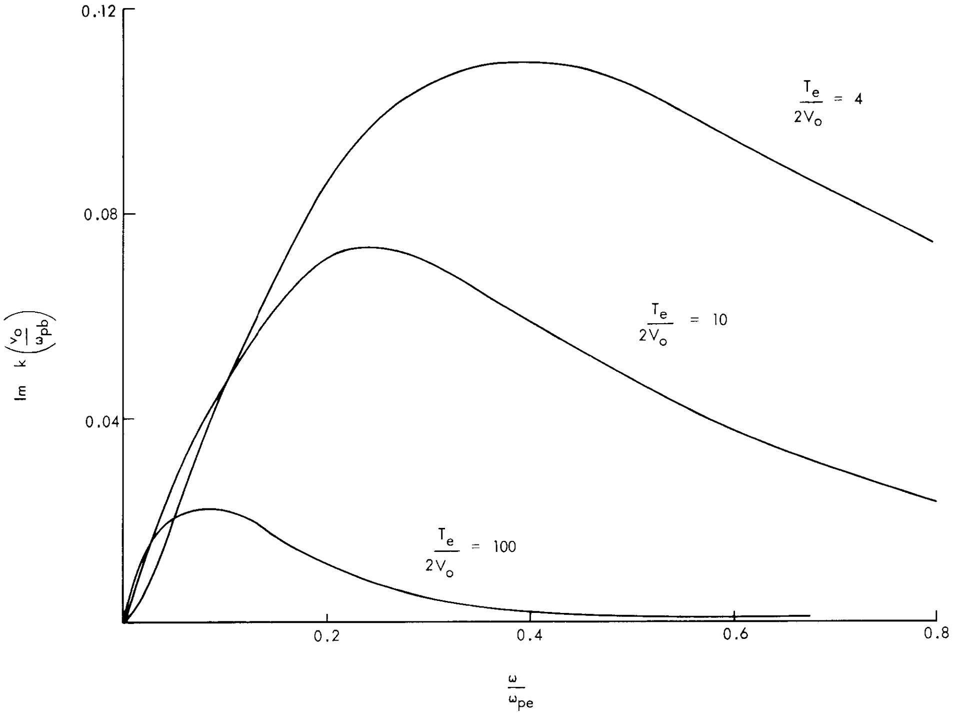

Fig. VII-13. Resistive-medium amplification.

b. Strong Beam

If the beam density is large enough so that $(n_b/n_p)(T_e/2V_o) > 1$, a very interesting transition takes place. This transition can be anticipated by looking at $k \to \infty$ as $\omega \to \omega_{pi}$;

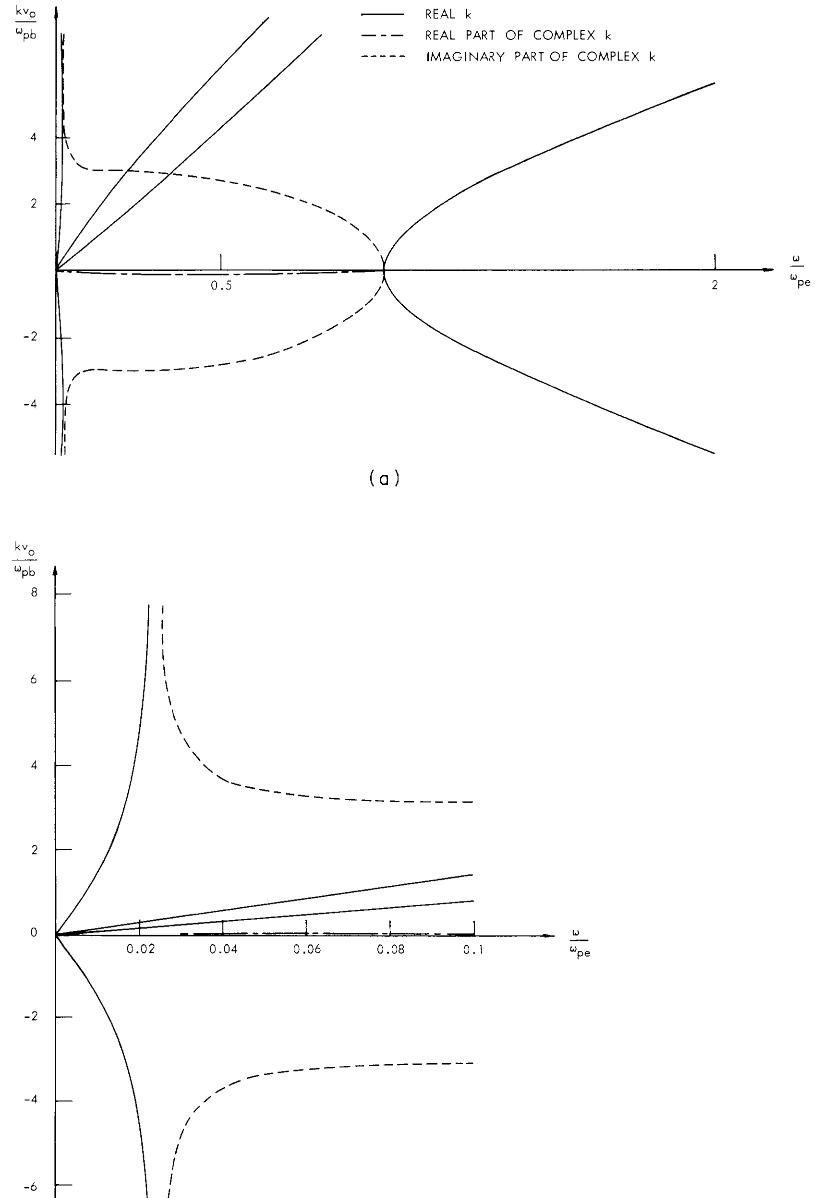

Fig. VII-14. (a) Longitudinal dispersion $n_b/n_p = 10^{-2}$, $T_e/2V_o = 10$.
(b) Detail at low frequency.

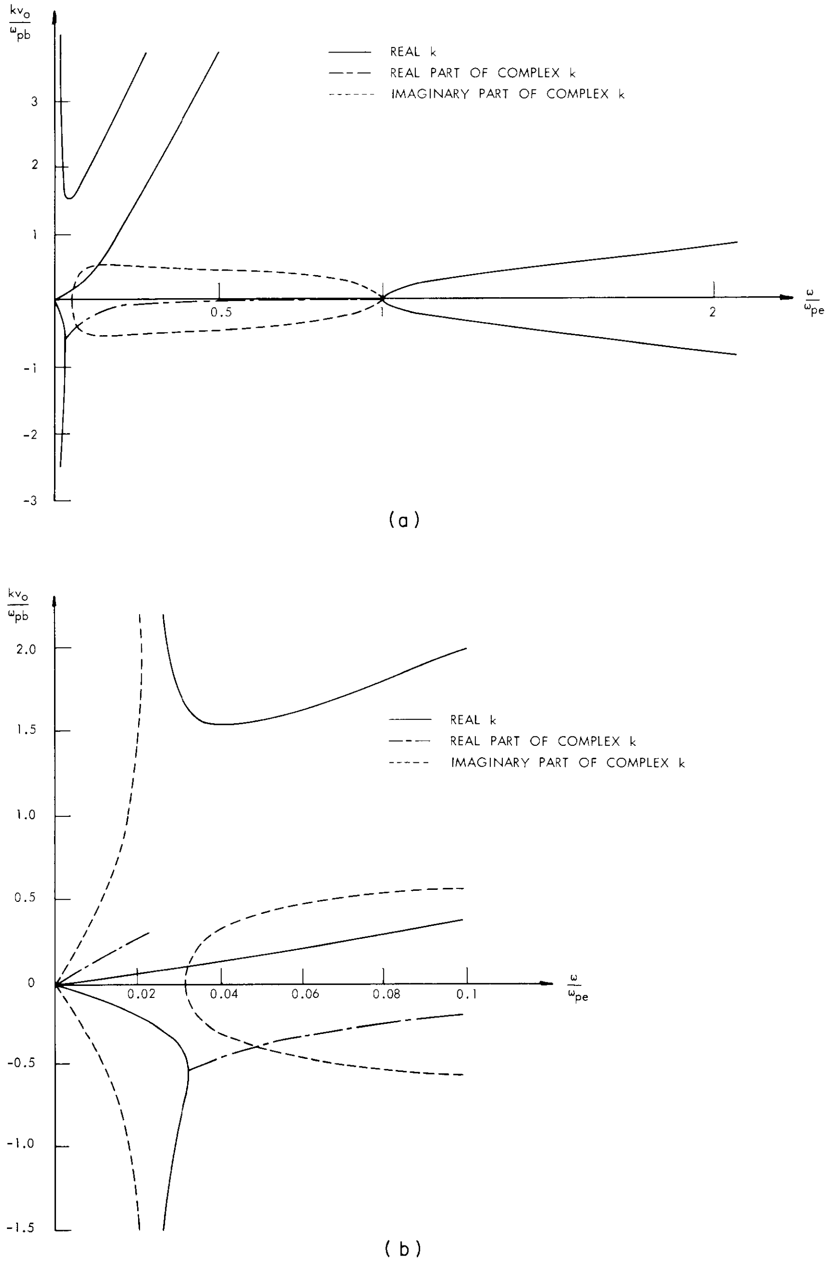

Fig. VII-15. (a) Longitudinal dispersion $n_b/n_p = 10^{-2}$, $T_e/2V_o = 400$.
(b) Detail at low frequency.

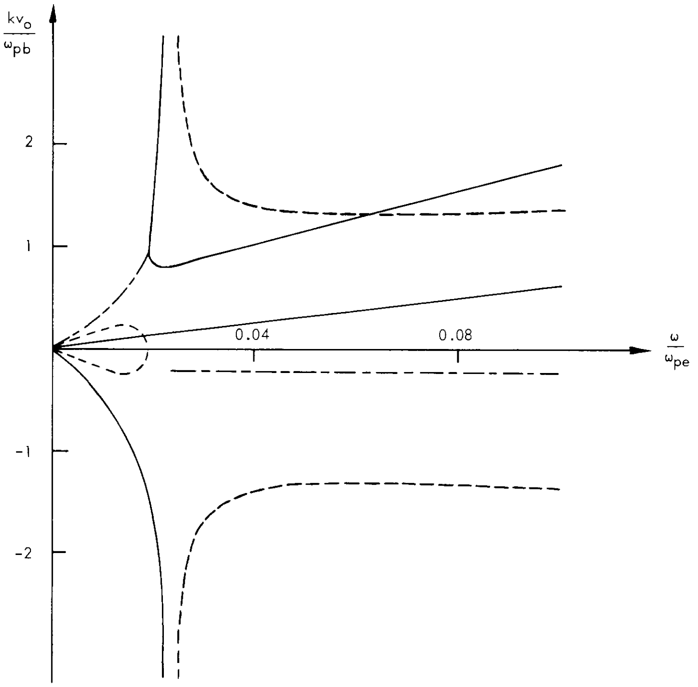

Fig. VII-16. Longitudinal dispersion $n_b/n_p = 10^{-2}$, $T_e/2V_o = 50$.

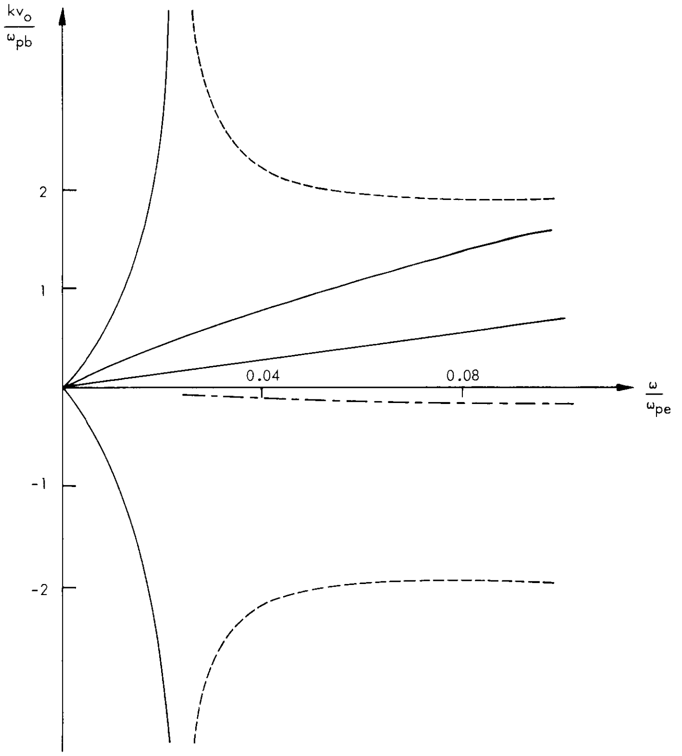

Fig. VII-17. Longitudinal dispersion $n_b/n_p = 10^{-2}$, $T_e/2V_o = 25$.

$$\frac{1}{k^2}\left[\frac{\omega_{pe}^2}{V_{Te}^2} - \frac{\omega_{pb}^2}{v_o^2}\right] = \frac{\omega_{pi}^2}{\omega^2} - 1. \tag{6}$$

We see that for $(n_b/n_p)(T_e/2V_o) > 1$, real k with $k \to \infty$ is obtained for $\omega > \omega_{pi}$ rather than $\omega < \omega_{pi}$. In Fig. VII-14, the complete dispersion is presented with the pressure formulation used for simplicity and with a proton plasma having the system parameters $n_b/n_p = 10^{-2}$ and $(n_b/n_p)(T_e/2V_o) = 0.1$. In Fig. VII-14, ω is real for all real k and the complex roots of k represent evanescent waves. In Fig. VII-15 the dispersion is plotted for $(n_b/n_p)(T_e/2V_o) = 4$; we see that now complex ω for real k is obtained (by counting the real roots), and the complex roots of k occurring for $\omega \leq \omega_{pi}$ now represent a convective instability with the spacial growth rate tending to infinity at $\omega = \omega_{pi}$.

If $(n_b/n_p)(T_e/2V_o)$ is only slightly less than one, there is still a convective instability but the spacial rate of growth is no longer infinite. This transition is illustrated in Figs. VII-16 and VII-17, in which the low-frequency dispersion is plotted for $(n_b/n_p)(T_e/2V_o) = 0.5$ and 0.25. We see that the instability has disappeared in the latter case (Fig. VII-17).

The condition for infinite gain at ω_{pi} can also be written as $\lambda_{pb} < \lambda_D$, where $\lambda_{pb} = 2\pi v_o/\omega_{pb}$ is the space-charge wavelength and $\lambda_D = 2\pi V_{Te}/\omega_{pe}$ is the Debye length in the plasma. This form is physically appealing, since it suggests that the "beam wavelength" should fit inside a Debye sphere in order to have strong interaction with the ions.

2. Transverse Interactions

The dispersion equation for the transverse waves splits into separate equations for right and left circularly polarized waves. From a collisionless kinetic treatment, assuming an isotropic equilibrium velocity distribution, one obtains

$$\frac{k^2c^2}{\omega^2} = 1 - \sum \frac{\omega_p^2}{\omega}\int \frac{f_o(\bar{v})\, d^3v}{\omega - kv_z \mp \omega_c} - \frac{\omega_{pb}^2(\omega - kv_o)}{\omega^2(\omega - kv_o \pm \omega_{ce})}, \tag{7}$$

where the sum is over all species of the plasma, and ω_{ce} and ω_{ci} are the electron- and ion-cyclotron frequencies, respectively. For a relativistic beam, the relativistic (transverse) mass should be used in computing ω_{pb} and the ω_{ce} of the beam, that is,

$$m = \frac{m_o}{\left(1 - \frac{v_o^2}{c^2}\right)^{1/2}}, \tag{8}$$

where m_o is the rest mass. It should also be noted that the inclusion of temperature by means of the transport equations with an isotropic pressure would predict no effect of temperature, since there is no bunching associated with the transverse waves.

a. Cold Plasma

The transverse wave interactions in a cold plasma were considered in Quarterly Progress Report No. 67 (pages 80-83). In that report, the conditions for charge neutrality were not carefully considered; consideration of these conditions here leads to a slight change in the very low frequency nonconvective instability. For a cold plasma, Eq. 7 becomes

$$\frac{k^2c^2}{\omega^2} = 1 - \frac{\omega_{pe}^2}{\omega(\omega\pm\omega_{ce})} - \frac{\omega_{pi}^2}{\omega(\omega\mp\omega_{ci})} - \frac{\omega_{pb}^2(\omega-kv_o)}{\omega^2(\omega-kv_o\pm\omega_{ce})}. \tag{9}$$

Requiring that the ion density in the plasma just equal the beam density plus the plasma electron density, and assuming that $\omega \ll \omega_{ci}$ and $kv_o \ll \omega_{ce}$, for the left polarized wave we obtain for Eq. 9

$$\omega^2 = k(k-k_o)\, u_a^2, \tag{10}$$

where u_a is the Alfvén speed in the plasma, $k_o = \mu_o J_{ob}/B_o$, J_{ob} is the beam current density, and we have assumed that $u_a \ll c$. This expression is a valid approximation for $k \leqslant k_o$ if $k_o \ll \omega_{ce}/v_o$, which requires that $\left(\omega_{pb}^2/\omega_{ce}^2\right)\left(v_o^2/c^2\right) \ll 1$. This dispersion is plotted in Fig. VII-18; we see that complex ω is obtained for real k between zero and k_o, whereas k is real for all real ω in this region; these results indicate a nonconvective instability. It can be shown that for such an instability to be excited, the length of the system much exceed a certain critical "starting length." For perfect electric conductors terminating the system, the shortest starting length is given by

$$L_{start} = \frac{2\pi}{k_o} = \frac{2\pi B_o}{\mu_o J_o}. \tag{11}$$

It is interesting to note also that this instability corresponds to a pure exponential growth in time of an initial spacial pattern of particle velocities.

An analysis of the right polarized wave shows that a similar nonconvective instability is obtained, only with $-k_o$ appearing in Eq. 10. It is easily shown that this represents exactly the same physical phenomena.

b. Warm Plasma

It can be shown that the electron temperature has essentially no effect on the convective instability near ω_{ci}, as would be expected physically. From Eq. 7 we see that for the ion temperature to be neglected it is necessary that $kV_{Ti} \ll \omega_{ci} - \omega$ near the

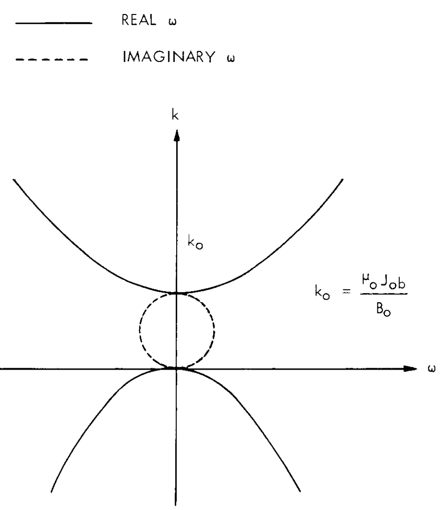

Fig. VII-18. Low-frequency transverse instability (left polarized).

intersection of the plasma wave and the beam cyclotron wave, where V_{Ti} is the average thermal velocity of the ions. This requires that

$$\frac{MV_{Ti}^2}{mv_o^2} \ll \frac{m}{M}\left(\frac{v_o}{c}\right)^4\left(\frac{\omega_{pi}}{\omega_{ce}}\right)^4. \tag{12}$$

(As an example, for protons of density 10^{12}/cc, magnetic field of 1000 gauss, and $v_o/c = 0.2$, Eq. 12 requires that the ion temperature be less than 10^{-7} volts, or much less than 1°K.) We conclude that for most cases of practical interest the ion temperature cannot be neglected in discussing the interaction at the ion-cyclotron frequency.

One finds, however, that there is still a convective instability near $\omega = \omega_{ci}$ when the ion temperature is included in Eq. 7. This interaction is again of a "resistive-medium" type, the physical origin of the "loss" mechanism now being the cyclotron damping in the plasma. For reasonable ion temperatures, such that the inequality of Eq. 14 is reversed, the maximum growth rate in space is

$$\text{Im } k = \sqrt{\frac{\pi}{2}}\,\frac{\omega_{ci}}{V_{Ti}}\,\frac{\omega_{pi}^2\omega_{pb}^2}{\omega_{ce}^4}\left(\frac{v_o}{c}\right)^4. \tag{13}$$

(For the example cited below Eq. 14, by assuming a beam density of 10^{10}/cc and ions of 0.1 ev, this growth rate is of the order of 10^{-5}/cm, which is a very weak amplification.)

The effect of temperature on the nonconvective instability, Eq. 10, is quite small, as would be expected, since the frequency is far from resonance. To neglect temperature effects, it is sufficient to require (see Eq. 7) that kV_{Te}/ω_{ce} and kV_{Ti}/ω_{ci} be much less than one for the maximum wave number that must be considered. This requires that

$$\frac{T_i}{2V_o} = \frac{MV_{Ti}^2}{mv_o^2} \ll \frac{M}{m}\left(\frac{u_a}{v_o}\right)^4\left(\frac{n_p}{n_b}\right)^2 \tag{14}$$

$$\frac{T_e}{2V_o} = \frac{mV_{Te}^2}{mv_o^2} \ll \left(\frac{M}{m}\right)^2\left(\frac{u_a}{v_o}\right)^4\left(\frac{n_p}{n_b}\right)^2. \tag{15}$$

(As an example, for protons in a magnetic field of 1000 gauss, beam density of 10^{10}/cc, and $V_o = 10^4$ volts, inequalities (14) and (15) are satisfied for ion temperatures less than 4×10^5 volts and electron temperatures less than 8×10^8 volts.)

It might be expected that collisions would have an important effect on this nonconvective instability, since ω is so small; however, it can be shown that the starting length is not altered if a relaxation type of collision frequency is included, although the peak growth rate in time is reduced.

R. J. Briggs, A. Bers

References

1. See, for example, the following review articles: F. W. Crawford and G. S. Kino, Proc.IRE 49, 1767-1789 (1961); Ya. B. Fainberg, J. Nuclear Energy, Part C 4, 203 (1962).

2. See, for example, A. I. Akhiezer and Ya. B. Fainberg, Soviet Phys. – JETP 21, 1262-1269 (1951); G. D. Boyd, L. M. Field, and R. W. Gould, Proc. Symposium on Electronic Waveguides (Polytechnic Institute of Brooklyn, Brooklyn, New York, 1958), pp. 367-375; V. S. Imshennik and Yu. I. Morozov, Soviet Phys. – Tech. Phys. 6, 464-471 (1961); and M. A. Lampert, J. Appl. Phys. 27, 5-11 (1956).

3. C. K. Birdsall, G. R. Brewer, and A. V. Haeff, Proc. IRE 41, 865-875 (1953).

G. SCATTERING OF LIGHT FROM (PLASMA) ELECTRONS III

By using slight improvements in the techniques developed in a previously reported electron-beam experiment,[1, 2] we have observed scattered optical radiation from the electrons in a dc thermal plasma. Development of these techniques will provide a powerful plasma diagnostic tool, since it is possible to obtain detailed measurements of the velocity distribution and density of the plasma electrons. These measurements can be made with very high spatial resolution (~1 mm^3); also, time resolution of these quantities should not present any great problems. Furthermore, this information is obtained without the introduction of probes, or, as is the case in some spectroscopic

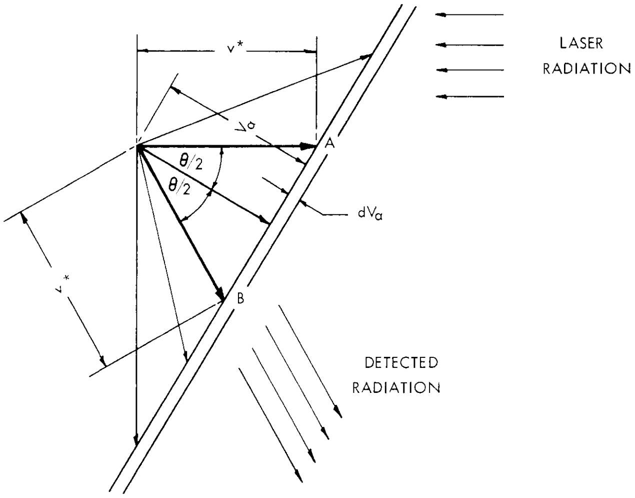

Fig. VII-19. Diagram used in derivation of spectrum of scattered radiation.

measurements, any impurity gases.

The derivation of the expected spectrum is made as follows. Consider an electron in velocity space at A with velocity equal to v^* (see Fig. VII-19); then this electron will "see" an input wavelength from the laser which is Doppler-shifted by an amount, $\Delta\lambda_1 = \lambda_0 - \lambda_1$ and is obtained from the well-known formula

$$\lambda = \lambda_0\left(1 \pm \frac{v}{c}\right).$$

(λ_0 is the input wavelength and λ is the wavelength observed by an observer moving with velocity v relative to the source of λ_0.)

This radiation is observed along the direction shown, and hence the observer will see radiation of wavelength λ_1 further Doppler-shifted by an amount depending on the component of velocity in the line of the detector. Let λ_2 be the wavelength of observed radiation.

Similarly, an electron at B with velocity equal to v^* will be observed to radiate at a wavelength λ_2 in the laboratory coordinates. We see, therefore, that all electrons whose velocity vector terminates on the extension of AB will be observed to give radiation shifted from the input wavelength by an amount $\Delta\lambda_2 = \lambda_0 - \lambda_2$.

The total number of such electrons is simply the number lying in that slice of velocity space dV_α thick and V_α away from the origin and is given by

$$dN_{V_\alpha} = Nf(V_\alpha)\, dV_\alpha,$$

where N is the total number of electrons, and f is the distribution function. For a Maxwell-Boltzmann distribution of electron velocities we have

$$dN_{V_a} = \frac{N}{\sqrt{\pi}}\left(\frac{m}{2kT}\right)^{1/2} \exp\left(-\frac{1}{2}\frac{mV_a^2}{kT}\right) dV_a,$$

which, in turn, can be written in terms of the wavelength shift $\Delta\lambda_2$ because

$$V_a^2 = \frac{V^{*2}}{2}(1+\cos\theta)$$

and

$$V^* = \frac{\Delta\lambda_2}{\lambda_o} c.$$

Hence

$$dN_{V_a} = \frac{N}{\sqrt{2\pi}}\left(\frac{m}{2kT_e}\right)^{1/2} \frac{c}{\lambda_o}(1+\cos\theta)^{1/2} \exp\left(-\frac{mc^2(1+\cos\theta)}{4k\lambda_o^2}\frac{\Delta\lambda_2^2}{T_e}\right) d\lambda,$$

where $d\lambda$ is the width of the filter used to select wavelength shift $\Delta\lambda_2$. For $\theta = 90°$ (the value used in our experiment) the expression simply reduces to

$$dN_{V_a} = A \exp\left(-\chi\frac{\Delta\lambda_2^2}{T_e}\right) d\lambda,$$

where

$$A = \frac{Nd\lambda}{\sqrt{2\pi}}\left(\frac{m}{2kT_e}\right)^{1/2} \frac{c}{\lambda_o}$$

and

$$\chi = \frac{mc^2}{4k\lambda_o^2}.$$

Hence a semi-log plot of signal amplitude versus $\Delta\lambda_2^2$ will give T_e for a Maxwell-Boltzmann distribution. The intensity of scattered radiation dI_s of wavelength λ_2 is

$$dI_s = \frac{I_o}{a}\left(\frac{e^2}{mc^2}\right)^2 \sin^2\phi \, d\Omega \, \frac{n_eV}{\sqrt{2\pi}}\left(\frac{m}{2kT_e}\right)^{1/2} \frac{c}{\lambda_o} \exp\left(-\chi\frac{\Delta\lambda_2^2}{T_e}\right) d\lambda$$

for plane polarized input, of intensity I_o in an area a. The angle ϕ is the angle between the plane of polarization and the direction of observation, and V is the volume in the field of view. Therefore, by making an absolute measurement of the intensity of scattered radiation, we can also determine the electron density n_e in the plasma.

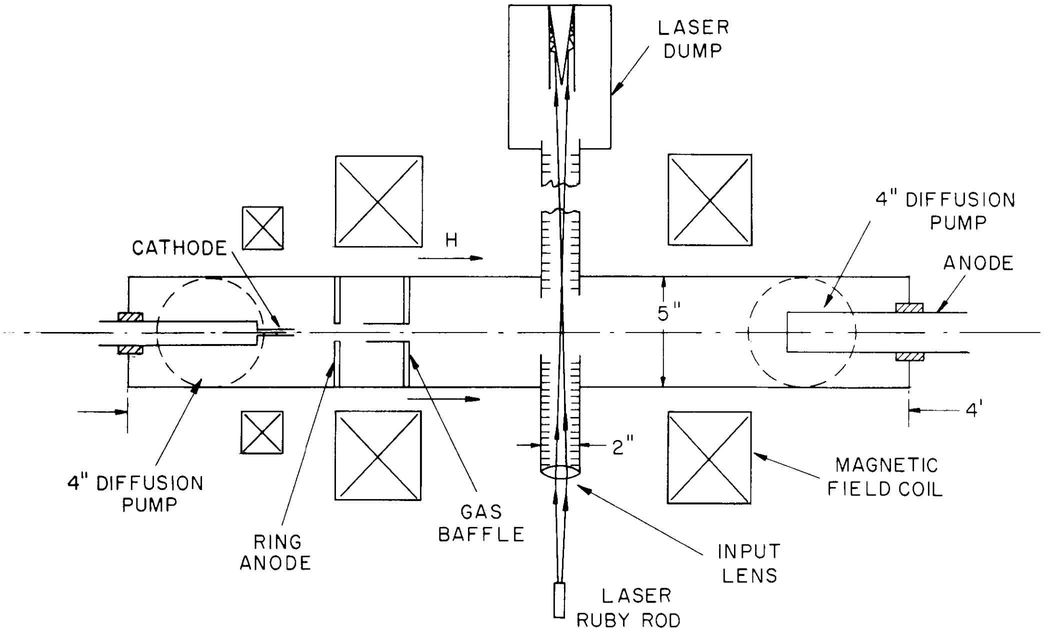

Fig. VII-20. Schematic diagram of apparatus. Plan view.

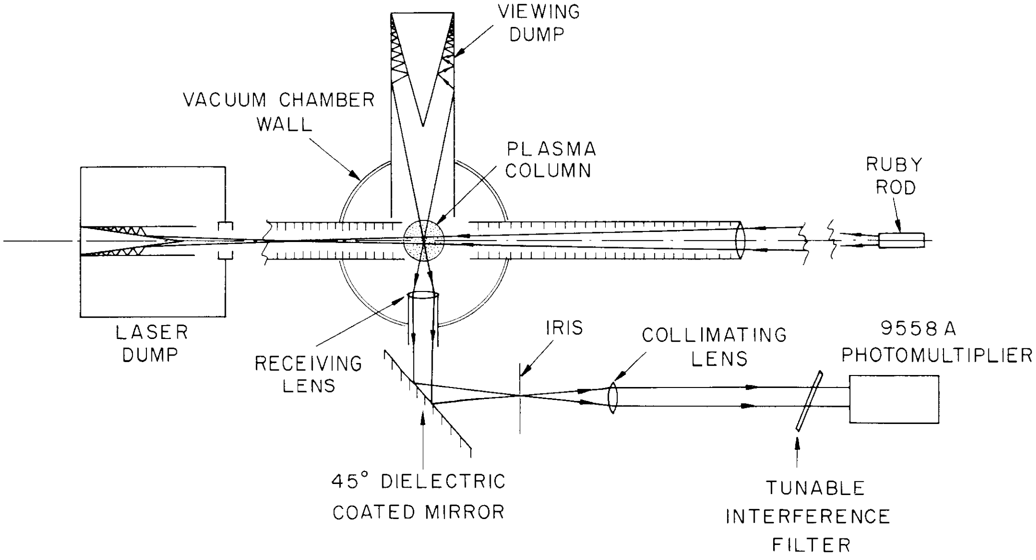

Fig. VII-21. Cross-section view of apparatus.

A schematic diagram of the apparatus is shown in Fig. VII-20 and a cross section through the plasma-laser interaction region is shown in Fig. VII-21. The plasma source is the hollow-cathode discharge developed in the Research Laboratory of Electronics, a full description of which has been given.[3] By using this device, an argon plasma with an electron density of $\sim 10^{13}$ electrons cm^{-3} and electron temperature of a few electron volts is produced along the axis of the machine. Twenty joules of light at 6934 Å from a ruby laser is passed through the plasma column before being absorbed in the specially designed dump chamber, the principle of which is evident from the diagram. A similar dump forms a black background for the receiving lens whose field of view is limited by the iris. The scattered radiation is collimated before reaching the tunable interference filter that has a 5 Å passband, the center of which is continuously variable from 6940 Å to 6700 Å. The detector is an EMI 9558 A photomultiplier.

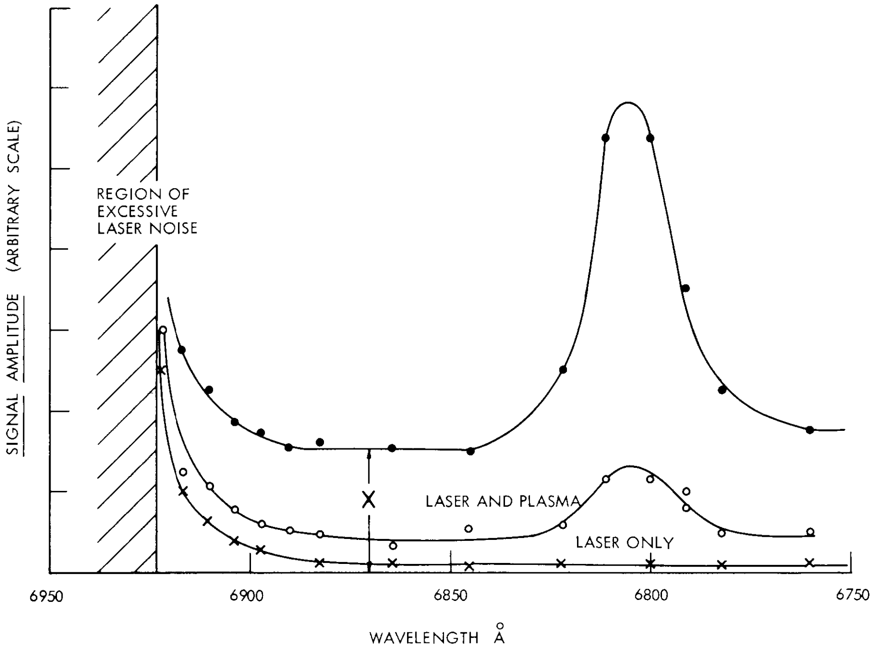

Fig. VII-22. Results of series 3 experiment (argon plasma stream).

The results of our first experiment (series 3), in which we obtained the spectrum of the scattered radiation, are given in Fig. VII-22 in which the amplitude of the detected signal (in arbitrary units) is plotted against wavelength. It is stressed, however, that these results are of a preliminary nature. The bottom curve is the spectrum obtained in the absence of plasma and represents the effect of radiation scattered from the walls of the vacuum chamber, and so forth, breaking through the filter. The middle curve shows the detector output when the laser is fired into the plasma, and the top curve represents the difference between these two curves on an expanded scale.

The shape of the top curve shows two peculiar effects:

(a) the peak centered at 6805 Å, and

(b) the curve does not go to zero in the wavelength range scanned.

It is difficult to attribute either of these effects to Thomson scattering from the

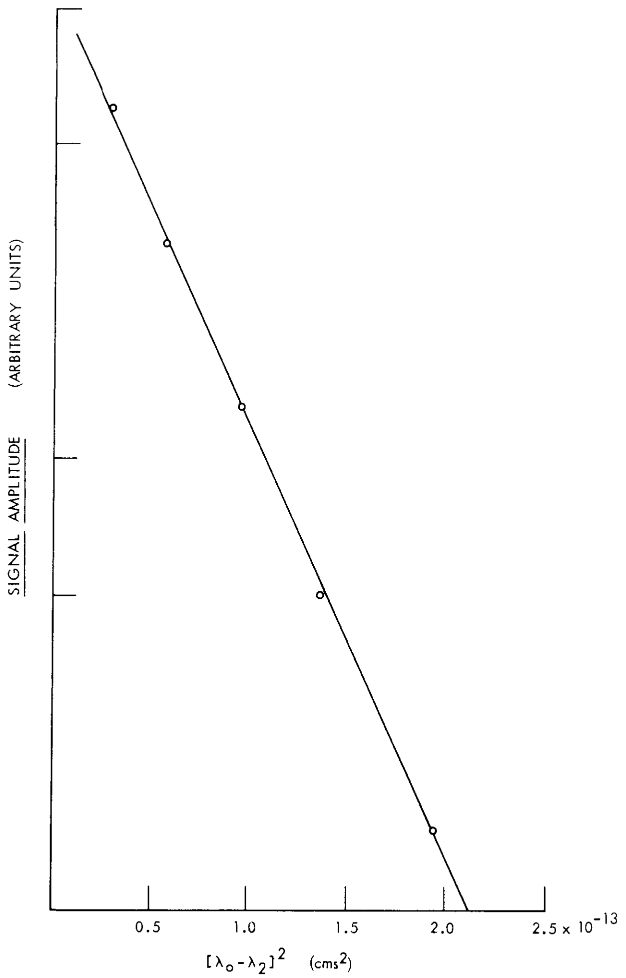

Fig. VII-23. Results of series 3 experiment.

plasma electrons, and it is tentatively suggested that these effects arise from the emission of radiation from the plasma as a result of the laser input. The large peak at 6805 Å is perhaps due to Raman scattering (the vibrational line being broadened by rotational lines).

We have some evidence to show that parts of the plasma emit radiation of fairly uniform intensity over a wide range of wavelengths ~0.2 msec after the laser pulse is turned on – this phenomenon suggests the idea of optical pumping of some levels in either excited states of A, A_2^+ or A^+ which then reradiate. If this unresolved effect of amplitude X is subtracted from the signal amplitude near the laser line, that is, we assume that there are no electrons present with energies greater than 10 ev, and plot signal amplitude versus $\Delta\lambda_2^2$, we obtain the result shown in Fig. VII-23. The value of electron temperature obtained from the gradient of this line is 1.2 ev.

E. Thompson, G. Fiocco

References

1. G. Fiocco and E. Thompson, Phys. Rev. Letters 10, 89 (1963).

2. G. Fiocco and E. Thompson, Scattering of light from electrons, Quarterly Progress Report No. 67, Research Laboratory of Electronics, M.I.T., October 15, 1962, pp. 90-91; and Quarterly Progress Report No. 68, pp. 74-76.

3. L. M. Lidsky, S. D. Rothleder, D. J. Rose, S. Yoshikawa, C. Michelson, and R. J. Mackin, Jr., J. Appl. Phys. 33, 2490-2497 (1962).

H. USE OF FISSILE NUCLIDES IN FUSION REACTOR BLANKETS

The preliminary investigation of this problem has been completed and a final report, in the form of an S.M. thesis to be submitted to the Department of Nuclear Engineering, M.I.T., is being prepared.[1]

The author's conclusions, based on tritium regeneration and heating-rate calculations, regarding the feasibility and the practicality of the three blanket configurations described previously[2,3] are as follows.

(a) The metallic thorium first-wall blanket assemblies are rejected on the ground that the thermal stress in the first wall limits the reactor operation to impractically low power levels.

(b) The blanket systems with depleted UF_4 fused salts in the first-wall coolant region are restricted to low-power operation (by heat transfer limitations arising from the liberation of from 77 per cent to 135 per cent of the incident neutron energy flux in the narrow coolant region).

(c) The blanket configurations containing a high UF_4 constituent (17-27 mole fraction percentage) fused salt in the primary attenuator with approximately 50 per cent Li^6 enrichment appear to be feasible and practical. The calculated tritium breeding ratios are in excess of 1.2; thus a self-sustaining tritium cycle is ensured. The heat-generation rates in the Mo first wall and in the coolant region are comparable to the nonfissile systems studied by Impink and Homeyer[4,5]; therefore operation at the same incident energy flux of from 4 to 5 $\frac{Mw}{m^2}$ is possible. The fast fission reaction doubles the recoverable energy liberated in the blanket, and approximately 90 per cent of the heat is generated in the large primary attenuator region. The manufacture of one plutonium 239 atom per five fusion reactions may have economic implications in terms of fission reactor fuel.

L. N. Lontai

References

1. L. N. Lontai, A Study of a Thermonuclear Reactor Blanket with Fissile Nuclides (S.M. Thesis, to be submitted to the Department of Nuclear Engineering, M.I.T., May 1963).

2. L. N. Lontai, D. J. Rose, and I. Kaplan, Use of fissile nuclides in fusion reactor blankets, Quarterly Progress Report No. 68, Research Laboratory of Electronics, M.I.T., January 15, 1963, pp. 77-82.

3. L. N. Lontai and A. J. Impink, Jr., Use of fissile nuclides in fusion reactor blankets, Quarterly Progress Report No. 67, Research Laboratory of Electronics, M.I.T., October 15, 1962, pp. 91-94.

4. A. J. Impink, Jr., Neutron Economy in Fusion Reactor Blanket Assemblies, Ph.D. Thesis, Department of Nuclear Engineering, M.I.T., January 1963.

5. W. G. Homeyer, Thermal and Chemical Aspects of the Thermonuclear Blanket Problem, Sc.D. Thesis, Department of Nuclear Engineering, M.I.T., December 1962.

I. FUSION REACTOR BLANKET EXPERIMENT

1. Introduction

Experiments have been initiated to study the neutronics of models of a tritium regenerating blanket to surround a power-producing deuterium-tritium cycle thermonuclear reactor. The objects of the experiments are (a) to check calculational methods[1-3] used to determine neutron fluxes and tritium production rates, and (b) to provide a versatile

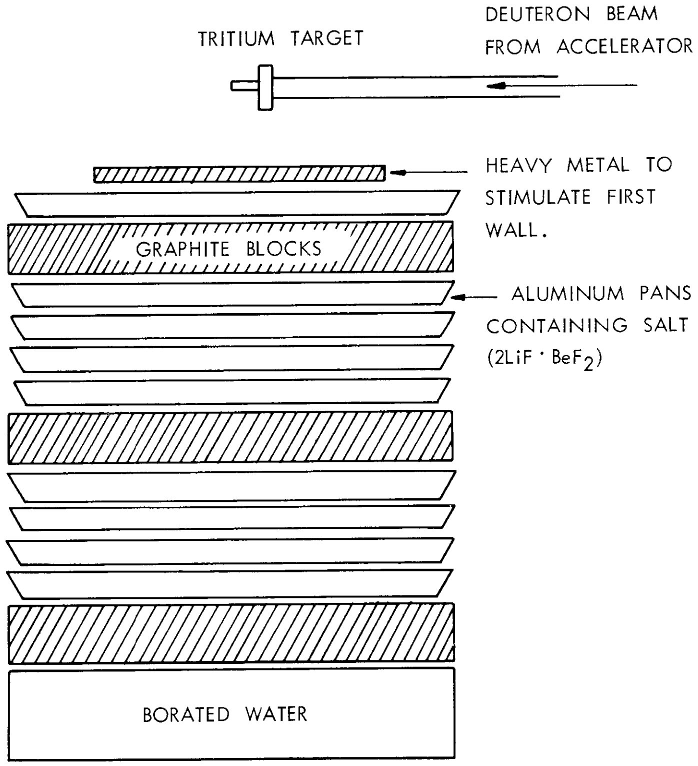

Fig. VII-24. Mock-up of a fusion reactor blanket.

means of studying effects of changes of materials and geometry on neutron flux and tritium production.

The blanket[2-5] is envisioned as a series of annular regions surrounding a cylindrical plasma, which contain materials for neutron multiplication and moderation, for removal of heat generated in the plasma and in the blanket, and for tritium production by the $Li^6(n, \alpha)H^3$ and $Li^7(n, n\alpha)H^3$ reactions. In the experiments, a core is removed from this blanket, and the resulting cylinder is irradiated with a point source of 14-Mev neutrons. A schematic diagram of the experimental arrangement is shown in Fig. VII-24.

2. Neutron Source

The 14-Mev neutrons for the experiment are supplied by a tritium gas target, shown in Fig. VII-25. The tritium is contained in a stainless-steel tube 1/4 inch ID and 1.3 inches long. The target window, a disc of commercial aluminum foil 33.8 μ thick, is

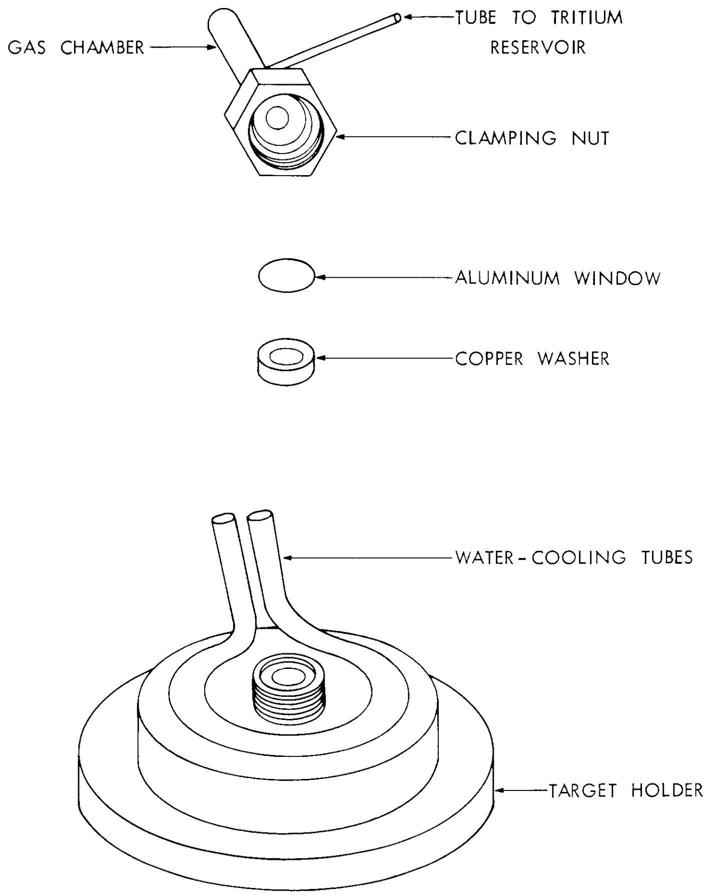

Fig. VII-25. Gas target.

held to the polished surface on a flange on the open end of the cylinder. A copper washer seals the window to the cylinder; the other side of the washer forms a seal with the target holder. Preliminary tests indicate that the window can withstand a 6-μa beam of 2.7-Mev deuterons almost indefinitely. The incident 2.7-Mev beam of deuterons is slowed to 400 kev in the window, whence it enters the gas chamber, where it is slowed to 40 kev. The calculated yield is 9×10^8 neutrons per second per microampere.

The tritium is supplied by a uranium tritide furnace similar to that described by Johnson and Banta.[6]

The 2.7-Mev deuterons are supplied by the Van de Graaff accelerator at the Air Force Cambridge Research Laboratory, Bedford, Massachusetts.

3. The Blanket Mock-Up

Most of the materials for the blanket, such as graphite for neutron-moderating regions, are available in sufficient quantities for the mock-up assembly. Approximately 300 lb of lithium-beryllium fluoride (composition $2LiF \cdot BeF_2$) to simulate the fused-salt regions have been supplied by the Reactor Chemistry Division of the Oak Ridge National Laboratory. The salt is sealed in 12 aluminum pans 18 inches in diameter, and 1 inch thick.

4. Tritium Counting

The tritium produced in the blanket assembly by the two lithium reactions is trapped in the crystal lattice of the lithium-beryllium fluoride. Salt samples will be melted in copper tube furnaces; the tritium thus evolved is swept into a proportional counter, by using a Teoppler pump to complete the transfer. A mixture of 10 per cent methane and 90 per cent argon is used as both the sweeping gas and the counting gas. After counting the tritium activity ($<10^5$ dpm) the gases in the proportional counter are exhausted outside the laboratory. Since tritium will build up in the bulk of the salt in the assembly from one experiment to another, fresh samples wrapped in aluminum foil will be used for counting in each experiment. By this method, the tritium production rate can be measured throughout the salt-containing regions of the assembly. The tritium-measuring system has been checked with salt samples irradiated by thermal neutrons in the M.I.T. reactor.

5. Threshold Detectors

a. Selection

The neutron flux in the blanket mock-ups will be measured as a function of position in the blanket and of the neutron energy by means of threshold detectors. After a search among publications five suitable threshold reactions were found: $U^{238}(n,f)$, $P^{31}(n,p)Si^{31}$, $Fe^{56}(n,p)Mn^{56}$, $I^{127}(n,2n)I^{126}$, and $F^{19}(n,2n)F^{18}$. Details of these detectors are given

Table VII-1. Threshold detector properties.

Element	Uranium	Phosphorus	Iron	Iodine	Fluorine
Reaction	$U^{238}(n, f)$	$P^{31}(n, p)Si^{31}$	$Fe^{56}(n, p)Mn^{56}$	$I^{127}(n, 2n)I^{126}$	$F^{19}(n, 2n)F^{18}$
Threshold Energy (Mev)	1.0	2.0	4.5	9.5	12.0
Half-life of daughter		2.62 hr	2.58 hr	2.6 hr (13 d)[a]	1.85 hr
"Effective" cross section[b]	990 mb	32.1 mb	34.9 mb	318.1 mb	21.0 mb
Material	Depleted metal foil	$Ca(PO_3)_2$ glass	Metal foil	PbI_2 or C_6I_6	Teflon (CF_2)
Competing reactions – Half-life of product		$(n, 2n)$-2.6 m (n, γ)-14.3 d	$Fe^{54}(n, \gamma)$-2.7 yr $Fe^{58}(n, \gamma)$-35 d	(n, γ)-25 m	(n, p)-29 s (n, α)-7.3 s (n, γ)-12 s
Radiation counted from main reaction	Integral γ	1.477 Mev β^-	845 kev γ	Integral β	650 kev β^+
References for cross-section curves	8	8, 9, 10	8, 11, 12, 13, 14, 15	8, 15, 16	16, 17, 18, 19, 20

[a] 2.6 hr is the internal transition half-life.

[b] Calculated for typical Impink spectrum.

in Table VII-1. Several factors had to be considered in choosing the reactions to be used.

Half-Life. Since it will require about one hour after a run with the accelerator to begin counting the foils, the half-life of the daughter products of the reactions that we use cannot be much less than 1 hour, or the activity produced will have decayed before it can be counted. On the other hand, if the half-life is much longer than several hours, not enough activity will be produced, unless the cross section for the reaction is very large. Also, the half-life of the daughters of the main reactions must be much longer or much shorter than those of competing reactions, so that either the competing activity can be allowed to decay before counting, or else the competing activity will be small.

Cross Section. The cross section for the reaction should be an accurately known function of energy in the region <16.5 Mev. This requirement eliminates most of the prospective reactions because (a) work with threshold detectors has usually been done for reactor systems, for which the highest energy of interest is ~2 Mev, and (b) a great deal of the data on threshold detectors results from measuring an effective cross section for a neutron energy spectrum that is almost a fission spectrum. From calculations made by Impink,[7] we conclude that the spectrum in the blanket assembly will be nothing

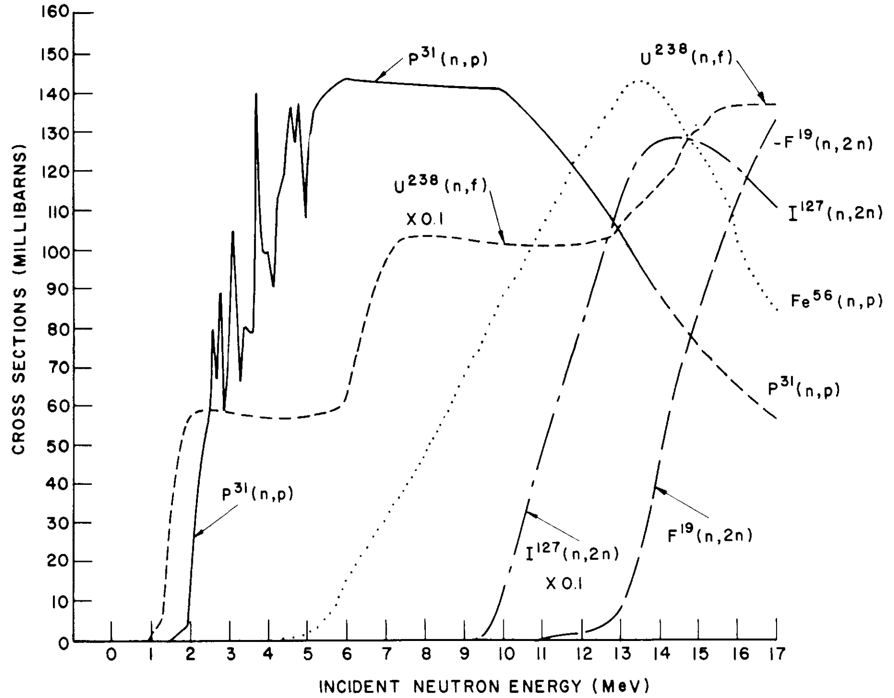

Fig. VII-26. Cross sections for threshold detector reactions. The curves shown are the best ones from available data (see Table VII-1). The curve for P^{31}(n, p) has been averaged over the resonances in the 2-5-Mev region; beyond 14 Mev, it was extrapolated on a logarithmic plot.

like a fission spectrum; hence data on effective cross sections are of no value in the present work.

The cross sections for the reactions used are shown in Fig. VII-26. In general, the cross sections are those of BNL-325 modified by later measurements.[8] Except for the reaction $F^{19}(n, 2n)F^{18}$, the cross sections measured by various authors are in good agreement. In the case of the fluorine reaction there are two widely varying sets of measurements of $\sigma(E)$, one by French[17] researchers, and one by Russians.[18] The Russian data are rather carefully documented, but the French values are simply presented as preliminary results; furthermore, the Russian data at 14 Mev are in better agreement with the work of others who have measured the cross section only at this energy. Hence the Russian data are used in this work.

For use as a threshold detector the cross sections for the $P^{31}(n, p)Si^{31}$ reactions have been averaged over the many narrow resonances in the 2-5 Mev region. The cross-section curve for this reaction is extrapolated logarithmically above 14 Mev, because of the lack of measurements in this region. The extrapolation seems reasonable from other (n, p) reactions that were studied.

Foil Material. To ease the problem of counting the foils after a given run, the parent isotope must be in a form that does not require special handling procedures. If a compound is to be used, the additional elements cannot contribute too much to the background. For uranium and iron, metal foils can be used to satisfy this requirement. The carbon in the Teflon that is used for the fluorine does not interfere, since the threshold energy for the $C^{12}(n, 2n)$ reaction (20 Mev) is above the maximum neutron energy that will be encountered in these experiments.

Although most authors suggest using ammonium phosphate as a phosphorous-containing foil, we find that calcium metaphosphate ($Ca(PO_3)_2$) is a better material.[21] The foils were manufactured as follows: Monobasic calcium phosphate powder ($Ca(H_2PO_4)_2 \cdot H_2O$) is heated in graphite crucibles to 2300°F, at which temperature it dehydrates, decomposes to $Ca(PO_3)_2$, and then melts. The resulting clear syrupy fluid is poured into graphite molds (which are heated by a hot plate), and pressed into shape, before molten fluid solidifies. The resulting clear glass pellets (3/4 inch in diameter, 1/8 inch thick) are annealed at 850°F for several hours to remove the thermal strains introduced in casting, and then slowly brought to room temperature. The pellets can then be handled as ordinary glass, although they are not quite so brittle. They are of approximately 90 per cent theoretical density, because of air bubbles and bits of graphite trapped during the casting process.

For the $I^{127}(n, 2n)I^{126}$ reaction, lead iodide[22] appears to be a suitable material. Hexaiodobenzene is also being investigated.

b. Analysis of Data

The analysis of the threshold foil data is based on an orthonormal polynomial expansion method of Lanning and Brown.[23] A FORTRAN II program has been written to perform the data analysis, and is now being tested with reaction rates calculated by Impink[7] used.

P. S. Spangler

References

1. W. G. Homeyer, A. J. Impink, Jr., D. J. Rose, and I. Kaplan, The fusion blanket problem, Quarterly Progress Report No. 62, Research Laboratory of Electronics, M.I.T., July 15, 1961, pp. 64-68.

2. W. G. Homeyer and A. J. Impink, Jr., Energy extraction blanket for a fusion reactor, Quarterly Progress Report No. 64, Research Laboratory of Electronics, M.I.T., January 15, 1962, pp. 128-131.

3. W. G. Homeyer, A. J. Impink, Jr., and D. J. Rose, Energy extraction blanket for a fusion reactor, Quarterly Progress Report No. 66, Research Laboratory of Electronics, M.I.T., July 15, 1962, pp. 142-150.

4. A. J. Impink, Neutron Economy in Fusion Reactor Blanket Assemblies, Sc.D. Thesis, Department of Nuclear Engineering, M.I.T., January 1963.

5. D. J. Rose and M. Clark, Jr., Plasmas and Controlled Fusion (The M.I.T. Press, Cambridge, Mass., and John Wiley and Sons, Inc., New York, 1961).

6. C. H. Johnson and H. E. Banta, Rev. Sci. Instr. **27**, 132 (1956).

7. A. J. Impink, Jr., Private communication, October 1962.

8. BNL-325, Brookhaven National Laboratory, Upton, New York, Second Edition, 1958, Supplement, 1960.

9. P. Cuzzorrea, G. Pappalardo, and R. Ricamo, Nuovo cimento **16**, 450 (1960).

10. J. Kantele and D. G. Gardner, Nuclear Phys. **35**, 353 (1962).

11. J. Depraz, G. Legros, and R. Salin, J. phys. radium **21**, 377 (1960).

12. S. Yasumi, J. Phys. Soc. Japan **12**, 443 (1957).

13. B. D. Kern, W. E. Thompson, and J. M. Ferguson, Nuclear Phys. **10**, 233 (1959).

14. D. M. Chittenden II, D. G. Gardner, and R. W. Fink, Phys. Rev. **122**, 860 (1961).

15. M. Bormann, S. Cierjacks, R. Lang Kau, and H. Neuert, Z. Phys. **166**, 477 (1962).

16. E. B. Paul and R. L. Clark, Can. J. Phys. **31**, 267 (1953).

17. C. W. Williamson and J. Picard, J. phys. radium **22**, 651 (1961).

18. O. D. Brill', N. A. Vlasov, S. P. Katinin, and S. L. Sokolov, Doklady Akad. Nauk S.S.S.R. **136**, 55 (1961).

19. L. A. Rayburn, Bull. Am. Phys. Soc., Ser. II **3**, 377 (1958).

20. V. J. Ashby, H. C. Catron, L. L. Newkink, and C. J. Taylor, Phys. Rev. **111**, 616 (1958).

21. L. H. Weinberg, R. P. Schuman, and B. A. Gottschalk, KAPL-1283 Knolls Atomic Power Laboratory, 1955.

22. V. W. Brideweser, S.M. Thesis, Department of Nuclear Engineering, M.I.T., June 1961.

23. W. D. Lanning and K. W. Brown, WAPD-T-1380, Bettis Atomic Power Laboratory, Pittsburg, Pennsylvania, 1961; see also Trans. Am. Nuclear Soc. 4, 267(1961).